Pergamon

Geochimica et Cosmochimica Acta, Vol. 66, No. 13, pp. 2445–2473, 2002

0016-7037/02 $22.00 + .00

PII S0016-7037(02)00848-7

The IAB iron-meteorite complex: A group, five subgroups, numerous grouplets, closely related, mainly formed by crystal segregation in rapidly cooling melts

J. T. WASSON*,[1] and G. W. KALLEMEYN

Institute of Geophysics and Planetary Physics, University of California, Los Angeles, CA 90095-1567, USA

(*Received August* 7, 2001; *accepted in revised form January* 21, 2002)

Abstract—We present new data for iron meteorites that are members of group IAB or are closely related to this large group, and we have also reevaluated some of our earlier data for these irons. In the past it was not possible to distinguish IAB and IIICD irons on the basis of their positions on element-Ni diagrams, but we now show that plotting the new and revised data yields six sets of compact fields on element-Au diagrams, each set corresponding to a compositional group. The largest set includes the majority (≈70) of irons previously designated IA; we christened this set the IAB main group. The remaining five sets we designate "subgroups" within the IAB complex. Three of these subgroups have Au contents similar to the main group, and form parallel trends on most element-Ni diagrams. The groups originally designated IIIC and IIID are two of these subgroups; they are now well resolved from each other and from the main group. The other low-Au subgroup has Ni contents just above the main group. Two other IAB subgroups have appreciably higher Au contents than the main group and show weaker compositional links to it. We have named these five subgroups on the basis of their Au and Ni contents. The three subgroups having Au contents similar to the main group are the low-Au (L) subgroups, the two others the high-Au (H) subgroups. The Ni contents are designated high (H), medium (M), or low (L). Thus the old group IIID is now the sLH subgroup, the old group IIIC is the sLM subgroup. In addition, eight irons assigned to two grouplets plot between sLL and sLM on most element-Au diagrams. A large number (27) of related irons plot outside these compact fields but nonetheless appear to be sufficiently related to also be included in the IAB complex.

Many of these irons contain coarse silicates having similar properties. Most are roughly chondritic in composition; the mafic silicates show evidence of reduction during metamorphism. In each case the silicate O-isotopic composition is within the carbonaceous chondrite range ($\Delta^{17}O \leq -0.3‰$). In all but four cases these are within the so-called IAB range, $-0.30 \geq \Delta^{17}O \geq -0.68‰$. Fine silicates appear to be ubiquitous in the main group and low-Au subgroups; this requires that viscosities in the parental melt reached high values before buoyancy could separate these.

The well-defined main-group trends on element-Au diagrams provide constraints for evaluating possible models; we find the evidence to be most consistent with a crystal segregation model in which solid and melt are essentially at equilibrium. The main arguments against the main group having formed by fractional crystallization are: a) the small range in Ir, and b) the evidence for rapid crystallization and a high cooling rate through the γ-iron stability field. The evidence for the latter are the small sizes of the γ-iron crystals parental to the Widmanstätten pattern and the limited thermal effects recorded in the silicates (including retention of albitic plagioclase and abundant primordial rare gases). In contrast, crystal segregation in a cooling metallic melt (and related processes such as incomplete melting and melt migration) can produce the observed trends in the main group. We infer that this melt was formed by impact heating on a porous chondritic body, and that the melt was initially hotter than the combined mix of silicates and metal in the local region; the melt cooled rapidly by heat conduction into the cooler surroundings (mainly silicates). We suggest that the close compositional relationships between the main group and the low-Au subgroups are the result of similar processes instigated by independent impact events that occurred either at separate locations on the same asteroid or on separate but compositionally similar asteroids.

1. INTRODUCTION

There are four large groups of iron meteorites. All researchers agree that three of these (IIAB, IIIAB, and IVA) formed by efficient fractional crystallization of a slowly cooling magma (Haack and Scott, 1993; Wasson and Richardson, 2001). Such large sets of irons that formed by fractional crystallization are designated magmatic groups. There is disagreement regarding the origin of IAB, the other large group. Some (Wasson et al., 1980; Choi et al., 1995) concluded that it is a nonmagmatic group formed as impact generated melts with only minor solid/liquid partitioning effects superposed. Others (Kracher, 1982, 1985; McCoy et al., 1993; Benedix et al., 2000) endorsed models involving the fractional crystallization of magmas. Kelly and Larimer (1977) envisioned IAB irons to be successive extractions of partial melts from a chondritic source.

Wasson (1999) and Wasson and Richardson (2001) called attention to the advantages both for taxonomy and for cosmochemical modeling of plotting data for the magmatic groups on element-Au diagrams, as compared to the traditional element-Ni diagrams. The chief advantage for those groups is that

* Author to whom correspondence should be addressed (j.twasson@ucla.edu).
[1] *Also at:* Department of Earth and Space Sciences and Department of Chemistry and Biochemistry.

the total Au range is much larger, but the relative uncertainties (including sampling effects) are as low or lower than those for Ni. As a result, trends in the magmatic groups are much better defined on element-Au than on element-Ni diagrams. In this paper we show that trends involving nonmagmatic group IAB and similar irons are also better resolved on element-Au diagrams even though the degree of Au fractionation is small compared to that observed in the magmatic groups. Our new data set shows that there are several closely related groups within what we now call the IAB complex.

2. ANALYTICAL TECHNIQUES, SAMPLES, AND RESULTS

We determined 13 elements (12 plus Fe) in metal by instrumental neutron-activation analysis (INAA) in replicate analyses; data for Fe were used for internal normalization. The procedures are those given by Wasson et al. (1989) except for two minor changes. The mean sample thickness is now 3.0 instead of 3.2 mm, and we now apply small (generally in the range 0.95 to 1.05) sample-specific corrections to make the Ni values in the first count agree better with those from the third and fourth counts (which are corrected to make Fe + Ni = 990 mg/g). We then choose a correction factor for the second count that is intermediate between that for the first and the mean corrections in the third and fourth counts. In most cases, concentrations of Ge were also determined on other samples by radiochemical neutron activation analysis (RNAA).

Although the INAA data were gathered over two-plus decades, significant improvements in the quality were achieved starting in 1986. As a result, some meteorites were restudied and the recent analysis given double weight in the determination of the mean. In most meteorites we had previously determined Ni by atomic-absorption spectrophotometry; in these cases the Ni means were calculated treating the previous mean as an additional replicate. We have also reevaluated some older analytical runs to incorporate more sophisticated corrections and, in a few cases, revised some standards to correct systematic errors.

In Table 1 the meteorites are listed alphabetically together with their group assignments. Mean compositions of IAB irons and related irons are listed in Table 2, and previously unreported individual analyses carried out in or after 1986 are listed in the Appendix. To facilitate comparison of Table 2 with the diagrams, the meteorites are sorted into the new groups (or sets) resulting from this study and are listed in order of increasing Au content within each subgroup.

Some of the means listed in Table 2 differ from published values because of minor changes in calibration, minor changes in the weighting of replicates, or (in rare cases) the discovery of arithmetic or copying errors. We estimate relative 95% confidence limits on the listed means to be 1.5 to 3% for Co, Ni, Ga, Ir, and Au; 4 to 6% for As and Ge; 7 to 10% for W (values >0.3 μg/g), Sb (>200 ng/g), Re (>50 ng/g), and Pt (>2 μg/g). Because much of the Cr is in minor phases (mainly chromite), sampling errors result in relative confidence limits on the mean ≥10%. In addition, there is an Fe interference in the determination of Cr resulting from the $^{54}Fe(n,\alpha)^{51}Cr$ fast-neutron reaction; our somewhat uncertain estimate of the level of interference is 6 μg Cr per g of Fe (Wasson and Richardson, 2001). Our data were not corrected for this interference.

In a few samples there is scatter among the Cu replicates. Although some of this may reflect contamination by Cu-base diamond blades, in a later discussion we suggest that the scatter mainly reflects stochastic sampling of metallic Cu grains that are sometimes found in IAB irons, mainly associated with FeS (El Goresy, 1965).

3. THE CLASSIFICATION OF IRONS BELONGING TO THE IAB COMPLEX

3.1. Some History

The roman numeral system of dividing iron meteorites into fields on the basis of Ga concentration was devised by Goldberg et al. (1951) and Lovering et al. (1957). When Wasson (1970) discussed the high-Ga meteorites, he restricted group I to fall within certain relatively narrow fields on Ge-Ga and Ge-Ni diagrams; his group I extended down to Balfour Downs, with 56 μg/g Ga and 194 μg/g Ge, but he noted that there were several additional irons that fell along an extrapolation of these fields to lower concentrations. Wasson (1974) designated the low-Ga, low-Ge irons in these extrapolated fields IB irons, and designated the irons in the original group I as IA irons. His view was that these were densely populated and thinly populated parts of a single genetic sequence. Our current, more complete data set shows this view to be incorrect in detail.

A small set of related irons was designated IC by Scott and Wasson (1976). This group mainly shares relatively high Ga and Ge contents with IAB, but does not have the high As, Au, and Sb contents of the latter group. At this time there is no reason to believe that these irons are closely related to IAB, and they will not be discussed further in this paper.

Groups IIIC and IIID were first described by Wasson and Schaudy (1971), who noted that the "groups may be related to each other." Scott (1972) combined the two groups and Scott and Bild (1974) noted that several properties of IIICD members paralleled those of IAB irons. Scott and Wasson (1975) agreed that the combined IIICD set was a single group.

Wasson et al. (1980) extrapolated IIICD element-Ni trends down to low Ni concentrations, reclassifying several low-Ni IAB irons as IIICD on the basis of Ir, Ga, and Ge values that plotted below the main IAB trend. Choi et al. (1995) continued this approach and reported a large body of new INAA data on IAB, IIICD, and related irons. Despite these additional high-quality data, they could resolve no compositional hiatus between IAB and IIICD on Ga-Ni, Ge-Ni, Ir-Ni, or other element-Ni diagrams; they therefore recommended "that the entire (IAB-IIICD) set be treated as a single group, but with the proviso that researchers measuring properties of possible taxonomic values should continue to . . . search for hiatus."

3.2. Compact Data Fields on Element-Au Diagrams; the IAB Main Group and Several Related Subgroups

The criteria we used to select iron meteorites with compositional links to IAB are best discussed after surveying the properties of the meteorites having the characteristic properties of this set of meteorites. These criteria are discussed in more detail in section 3.6. The main threshold values are: Au >1.3 μg/g, As >10 μg/g, Co >3.9 mg/g, Sb >180 ng/g, At the bottom of Table 2 we also list 3 irons that are IAB related (e.g., based on O-isotopic compositions) despite having low Au and As values. There may be other exceptions.

When we plotted our IAB elemental data against Au instead of Ni we found that, with a small number of exceptions, on element-Au diagrams except Ir-Au and Cr-Au, the data tended to form compact fields (and in most cases, linear arrays). Most of the original IAB members (i.e., those with Ga > 50 μg/g) form a densely populated cluster having ≈70 members; we will call this the IAB main group and give it the symbol IAB-MG (or MG when the context is clear).

The Ni-Au diagram (Fig. 1) proved to be the best suited to resolving this large set of irons into smaller sets of closely related irons. In addition to the IAB main group, five subgroups and two related grouplets are resolvable on this diagram. For

Table 1. Assignment of irons belonging to different categories within the IAB complex.

Meteorite	Group	Meteorite	Group	Meteorite	Group
Algarrabo (Ovalle)	un	Garden Head	sHH	Oscuro Mountains	MG
Algoma	sHL	Gay Gulch	sHH	Ozren	MG
Allan Hills ALHA77283	MG	Gladstone (iron)	MG	Pecora Escarp PCA91003	MG
Allan Hills ALHA76002	MG	Goose Lake	sLL	Persimmon Creek	sLM
Allan Hills ALHA80104	sHH	Grosvenor Mt GRO95511	sLL	Pine River	sLL
Annaheim	sLL	Grove Mtns 98003	un	Pitts	un
Anoka	sLM	Guangxi Coal Mine	MG	Pittsburg	MG
Aswan	un	Harlowtown	un	Pooposo	MG
Bahjoi	sLL	Hasparos	MG	Purgatory Peak A77006	MG
Balfour Downs	sLL	Hassi-Jekna	sHL	Qarat al Hanash	sHL
Ballinger (UCLA)	MG	Hope	MG	Quesa	un
Bischtübe	sLL	Idaho	MG	Reckling Peak A80226	sLL
Black Mountain	MG	Itapuranga	MG	Rifle	MG
Bocaiuva	np	Jaralito	MG	Rosario	MG
Bogou	MG	Jenkins	MG	San Cristobal	un
Bohumilitz	MG	Jenny's Creek	MG	Santa Catharina	un
Bolivia	MG	Kaalijarv	MG	Sarepta	MG
Britstown	un	Karee Kloof	sLL	Seeläsgen	MG
Burgavli	MG	Kendall County	un	Seligman	MG
Burkett	MG	Kofa	sHH	Seymour	MG
Burkhala	un	La Serena	MG	Shrewsbury	sLL
Caddo	un	Lamesa	sLM	Silver Crown	MG
Campo del Cielo	MG	Landes	MG	Soledade	MG
Canyon Diablo H	MG	Lewis Cliff LEW 86540	sLH	Smithville	MG
Canyon Diablo L	MG	Lexington County	MG	Sombrerete	sHL
Carlton	sLM	Lime Creek	un	Surprise Springs	sLL
Casey County	MG	Linville	sHH	Tazewell	sLH
Chebankol	sHL	Linwood	MG	Thiel Mtn (TIL91725)	un
Chuckwalla	MG	Livingston (TN)	un	Toluca	sLL
Colfax	un	Lonaconing	sHL	Twin City	un
Comanche (iron)	sLL	Lueders	MG	Udei Station	un
Cookeville	un	Magnesia	sHL	Uruacu	MG
Coolac	MG	Magura	MG	Vaalbult	MG
Copiapo	MG	Maltahöhe	sLM	Ventura	un
Cosby's Creek	MG	Mazapil	sLL	Victoria West	sHL
Cranbourne	MG	Mertzon	un	Waterville	un
Dayton	sLH	Mesa Verde Park	un	Wedderburn	sLH
Deelfontein	MG	Morasko	MG	Wichita County	MG
Deport	sLL	Mount Ayliff	MG	Wolsey	MG
Dongling	MG	Mount Magnet	sHH	Woodbine	un
Duel Hill (1873)	MG	Mundrabilla	un	Wooster	sLL
Dungannon	MG	Mungindi	sLM	Wu-Chu-Mu-Chin	un
Edmonton (KY)	sLM	Muzaffarpur	sHL	Yardea	MG
Egvekinot	sLM	Nagy-Vazsony	sLL	Yenberrie	MG
Elephant Mor EET83333	sLL	Nantan	MG	Yongning	un
Elephant Mor EET84300	un	New Leipzig	MG	Youndegin	MG
Elephant Mor EET87006	un	Niagara	sLL	Zacatecas (1792)	np
Ellicott	un	No We Africa NWA468	un	Zaffra	MC
Fairfield (OH)	MG	No We Africa NWA176	np	Zagora	un
Föllinge	sLH	Ocotillo	MG	Zapaliname	MG
Four Corners	un	Odessa (iron)	MG	Ziz	MG
Freda	sLH	Ogallala	sLL		
Gahanna	MG	Oktibbeha County	un		

See text for group abbreviations; un = ungrouped member of IAB complex; np = not plotted, outside Au limits on diagrams.

this reason we have devised a nomenclature for the subgroups based on their mean Ni and Au contents. As discussed in more detail later, the low-Au groups all seem to be closely related to one another, and there is some possibility that several come from the same parent body; the link between the high-Au subgroups and the main group is more tenuous. The discovery of these closely related groups raises serious nomenclature problems; after considerable thought and discussion, we propose to designate them subgroups within the IAB complex rather than independent groups. We will, however, sometimes use groups as a generic description when referring to the main group and one or more subgroups.

The five subgroups have 6 to 15 members. Three of these have Au contents similar to those in the main group, and two have resolvably higher Au contents. We designate the former low-Au (LAu) subgroups and the latter high-Au (HAu) subgroups. These are then further divided into high-, medium-, and low-Ni subgroups (HNi, MNi, LNi). Thus the low-Au subgroup with the highest Ni content (which mainly consists of the old group IIID) receives the designation IAB-sLAuHNi, but we

Table 2. Mean composition of the irons in the IAB complex. Data listed separately for the main group, the 5 subgroups, the 5 duos, and the 17 solos, and sorted in terms of increasing Au within each of the sets of irons.

Meteorite	sil[a]	Cr (μg/g)	Co (mg/g)	Ni (mg/g)	Cu (μg/g)	Ga (μg/g)	Ge (μg/g)	As (μg/g)	Sb (ng/g)	W (μg/g)	Re (ng/g)	Ir (μg/g)	Pt (μg/g)	Au (μg/g)
IAB main group														
Landes	ac	438	4.51	65.5	317	87.5	414	10.2	256	1.42	349	4.33	12.5	1.417
Burgavli		28	4.45	66.4	168	97.1	519	11.0		1.90	162	1.19		1.435
Duel Hill (1873)		19	4.60	67.0	163	99.4	442	11.8	287	1.51	391	4.32	8.6	1.439
New Leipzig		19	4.65	66.8	149	92.2	445	11.3	228	1.47	281	2.95		1.439
Cosby's Creek		25	4.46	64.7	154	93.1	449	11.4	270	1.82	344	2.72		1.445
Wolsey		43	4.52	66.2	137	92.8	428	10.5	320	1.56	447	4.86	10.3	1.457
Uruacu		29	4.65	64.3	145	89.6	357	11.6	270	1.25	327	3.36	8.8	1.458
Magura		23	4.62	64.4	136	95.6	483	10.3	175	1.65	327	3.65		1.461
Ziz		30	4.54	67.5	140	89.1	400	10.7	180	1.20	210	2.07	6.9	1.461
Sarepta		25	4.65	65.9	149	98.8	456	11.5	341	1.39	421	4.38		1.464
Soledade		21	4.57	67.8	147	98.6	440	11.1	320	1.40	393	3.90	9.7	1.465
Zapaliname		31	4.58	67.1	130	84.2		11.8	235	1.27	202	1.82	5.9	1.466
Chuckwalla		28	4.61	65.9	156	100.0	371	12.4	484	1.56	243	2.72	8.6	1.468
Itapuranga		28	4.68	65.2	131	96.0	478	11.5	262	1.33	242	2.57	9.7	1.472
Bolivia		21	4.64	67.0	157	97.3	397	11.3	294	1.33	226	2.06	8.1	1.482
Coolac		35	4.51	69.9	161	93.5	423	11.1	276	1.42	295	2.84	8.1	1.485
Yardea		20	4.44	70.2	185	88.1	361	10.7	278	1.30	369	4.21		1.487
Ballinger (UCLA)		26	4.61	67.8	148	87.8	341	12.1	336	1.25	320	3.20	6.4	1.490
Campo del Cielo	ac	38	4.58	66.8	140	93.0	394	11.8	270	1.31	370	3.55	7.6	1.490
Gladstone (iron)		20	4.71	65.6	153	91.8	418	11.3	289	1.46	321	2.95		1.490
Seligman		28	4.59	66.7	162	93.5	423	12.2	332	1.22	327	3.29	7.2	1.491
Allan Hills ALHA76002		40	4.48	68.0	153	93.7	420	11.3	318	1.55	287	2.56		1.500
Pecora Escarp		29	4.62	70.8	148	82.6	327	13.0	338	1.11	271	3.61	5.9	1.504
Lueders	ac	381	4.65	70.2	351	78.7	253	12.0	307	1.22	297	3.88	6.5	1.505
Morasko		<31	4.53	67.6	154	102.7	500	11.6	269	1.78	124	1.11		1.505
Linwood	ac	12	4.54	67.1	136	91.0	374	11.9	325	1.17	301	2.85		1.508
Hope		23	4.60	70.6	148	89.9	402	11.2	270	1.35	70	0.75		1.510
Black Mountain		23	4.66	64.2	128	95.9	464	12.0	271	1.43	338	2.92	4.6	1.515
Seeläsgen		24	4.54	65.9	159	102.8	493	10.7	250	1.85	108	1.14		1.523
Jaralito		32	4.68	66.6	148	88.9	376	11.9	294	1.21	166	1.50		1.526
Nantan		20	4.72	68.8	143	79.8	293	12.8	309	1.01	168	1.79	6.3	1.530
Canyon Diablo H[b]		26	4.63	69.3	148	82.1	323	13.0	296	1.06	253	2.42	6.1	1.534
Yenberrie		29	4.72	68.2	159	84.0	319	12.6	338	1.03	319	3.50	5.7	1.535
Pooposo		44	4.63	70.0	196	79.6	325	11.9	328	1.02	246	2.68		1.537
Fairfield, OH		19	4.70	67.2	143	80.7	329	13.1	373	1.03	161	1.79	5.8	1.537
Oscuro Mountains		22	4.51	68.9	179	79.7	359	12.1	266	1.19	283	2.97		1.538
Youndegin		26	4.70	68.3	145	84.5	330	13.0	280	1.07	217	2.15	5.4	1.540
Idaho		24	4.66	72.3	154	83.4	321	13.2	289	1.06	262	2.54	4.7	1.543
Cranbourne		26	4.60	68.2	139	83.8	372	13.1	350	1.18	168	1.73		1.550
Hasparos		27	4.66	66.1	154	104	486	12.4	311	1.73	506	5.59		1.550
Canyon Diablo L[b]	ac	24	4.65	69.3	150	83.0	330	13.0	308	1.07	234	2.19	6.3	1.552
Lexington County		20	4.58	68.4	154	82.4	316	13.8	295	1.12	293	2.86		1.555
Jenny's Creek		22	4.71	68.8	141	82.2	322	13.6	361	1.13	272	2.41	5.9	1.559
Rosario		23	4.69	70.6	151	90.0	401	12.1	280	1.16	191	1.90		1.559
Seymour		29	4.68	67.8	159	87.2	381	12.8	231	1.15	194	1.74		1.562
Wichita County		32	4.66	67.9	148	83.4	342	12.4	373	1.20	210	1.90		1.565
Deelfontein		27	4.49	70.3	160	84.4	306	14.3	336	1.90	150	1.56	4.6	1.576
Jenkins		25	4.55	69.2	151	87.7	353	13.1	344	1.28	247	2.16		1.580
Guangxi Coal Mine		24	4.61	70.7	165	84.6	380	13.5	350	1.02	188	1.84	5.3	1.582
Silver Crown		28	4.61	71.6	142	83.4	321	12.8	312	1.01	289	2.81		1.585
Ozren		31	4.75	70.9	139	78.5	280	14.1	280	1.02	204	2.59	4.8	1.586
Rifle		24	4.69	70.5	134	77.2	281	14.4	340	0.88	211	1.94	4.3	1.587
Purgatry Pk PGPA77006		22	4.69	72.4	148	78.8	279	14.8	426	0.96	224	2.21	5.5	1.592
Bohumilitz		21	4.76	72.8	134	76.7	264	15.4	358	0.88	218	2.04		1.595
Vaalbult		26	4.52	68.3	145	83.6	333	14.8	—	1.24	281	2.14		1.595
Gahanna		16	4.63	69.3	174	85.4	282	13.1	370	0.96	232	1.87	6.0	1.597
Smithville		20	4.65	69.2	160	87.1	363	13.8	338	1.05	198	1.88	5.7	1.610
Odessa (iron)	gr	34	4.72	71.9	129	75.0	279	14.3	311	0.98	242	2.38	5.8	1.611
Dongling		22	4.73	71.2	157	87.8	239	13.9	761	1.02	143	1.71	4.0	1.615
Burkett		23	4.64	69.6	170	89.2	370	13.5	510	1.48	267	2.48		1.619
Casey County		22	4.73	69.7	163	81.2	318	13.7	400	1.24	155	1.35		1.620
Pittsburg		16	4.68	65.4	130	89.2	359	14.6	291	1.08	234	2.12	6.4	1.630
Mount Ayliff		26	4.88	73.5	134	80.0	267	15.7	287	0.86	262	2.24	6.9	1.633

(continued)

Table 2. (Continued)

Meteorite	sil[a]	Cr (μg/g)	Co (mg/g)	Ni (mg/g)	Cu (μg/g)	Ga (μg/g)	Ge (μg/g)	As (μg/g)	Sb (ng/g)	W (μg/g)	Re (ng/g)	Ir (μg/g)	Pt (μg/g)	Au (μg/g)
IAB main group, continued														
Bogou		23	4.67	73.3	163	78.5	301	14.2	304	1.09	194	1.72	4.8	1.645
Copiapo	ac	121	4.74	72.9	165	72.6	252	14.4	326	0.92	287	3.05		1.650
Dungannon		27	4.72	69.5	153	78.8	332	13.6	351	0.95	242	2.58	6.0	1.650
Kaalijarv		23	4.76	75.5	159	80.2	293	17.0	573	0.94	246	3.04	6.0	1.665
La Serena		16	4.76	76.2	181	70:5	204	15.9	352	0.66	<70	0.55	3.3	1.665
Ocotillo	ac, n	22	4.65	70.9	116	72.3	268	13.7	313	0.81	256	2.61	5.5	1.665
Zaffra		24	4.82	73.1	149	72.3	244	15.1	312	0.72	<30	0.062		1.665
Allan Hills ALHA77283		23	4.87	72.8	145	81.1	320	15.4	399	1.06	226	2.16	7.0	1.707
subgroup sLL (low Au, low Ni)														
Annaheim		23	4.74	77.9	494	79.6	301	13.4	381	1.17	372	3.52		1.555
Katee Kloof		35	4.71	82.0	231	80.0	355	15.0	475	1.27	103	1.30	7.0	1.580
Pine River	ac	11	4.92	80.4	215	74.1	234	15.7	376	0.69	305	3.06	5.0	1.635
Goose Lake		31	4.86	82.4	172	69.4	305	16.4	391	1.07	210	2.15	5.9	1.636
Ogallala		30	4.84	79.2	149	68.1	266	15.9	341	1.07	270	2.43	5.7	1.636
Wooster		18	4.82	78.1	174	66.2	258	15.2	308	0.85	250	2.58		1.650
Surprise Springs		37	4.85	80.0	193	69.4	264	16.0	393	0.78	252	2.37	4.6	1.654
Deport		21	4.73	80.5	177	64.8	255	17.2	419	1.12	263	2.37		1.685
Bischtübe		23	4.92	77.8	136	67.9	238	16.9	359	0.68	210	2.30	5.7	1.687
Balfour Downs		22	4.87	83.8	161	58.6	194	16.6	403	1.14	242	2.17	5.5	1.695
Grosvnr Mtn GRO95511		19	4.86	81.8	196	72.8	248	16.3	348	0.86	186	1.99	6.2	1.695
Mazapil		13	4.99	88.8	206	60.2	221	18.0	381	0.70	417	5.59	10.1	1.695
Toluca	ac,gr	23	4.90	80.2	170	68.9	245	16.5	380	0.83	250	2.47	5.7	1.718
Comanche (iron)		19	4.99	82.4	176	76.3	270	17.0	429	0.89	227	2.82	6.1	1.720
Recklng Pk RKPA80226		23	4.88	82.6	173	67.6	255	17.0	450	0.90	222	2.06		1.740
Elephant Mor EET83333	ac	19	4.88	80.6	184	74.8	226	15.7	459	0.80	274	2.88	6.8	1.750
Shrewsbury		16	4.88	85.3	217	62.6	196	17.3	431	0.61	260	2.77		1.750
Bahjoi		21	4.83	79.4	146	69.7	273	17.1	540	0.96	290	2.54	5.6	1.754
Niagara		14	5.01	79.3	172	72.0	266	16.7	402	0.80	272	2.71	5.1	1.757
Nagy-Vazsony		18	4.99	80.9	189	72.2	237	18.2	421	0.82	277	2.43	6.1	1.776
subgroup sLM (low Au, medium Ni; originally IIIC)														
Persimmon Creek	sr,ac	41	5.48	137.9	382	33.2	78.3	15.8	624	0.23	112	0.852		1.535
Maltahöhe	ac	15	5.26	114.0	163	24.0	38.5	19.2	483	0.20	<50	0.17	1.9	1.600
Anoka		21	5.56	118.0	197	17.8	15.7	21.4	477	0.11	<30	0.172	1.2	1.617
Mungindi		15	5.50	118.6	248	18.8	22.2	22.4	481	<0.0	76	0.583	1.4	1.665
Edmonton (KY)		21	5.48	129.0	404	24.2	34.3	21.3	467	0.29	<100	0.457		1.705
Carlton	ac	18	5.67	132.3	260	11.9	8.59	23.5	520	<0.2	<50	0.082		1.737
Lamesa		12	5.60	132.8	323	13.1	11.9	24.2	684	<0.1	<30	0.045	<0.6	1.754
Egvekinot		11	5.62	143.0	359	12.6	10.2	25.1	616	0.18	<50	0.098		1.830
subgroup sLH (low Au, high Ni; originally IIID)														
Föllinge		12	5.96	177.9	371	3.88	3.15	26.4	838	<0.0	<20	0.11	<1.1	1.700
Dayton	ac	12	5.92	171.0	435	4.85	3.41	25.2	684	<0.2	<50	0.03	1.4	1.736
Tazewell		13	5.89	170.6	391	4.75	3.78	26.6	682	<0.10	<20	0.10		1.763
Lewis Cliff LEW 86540		12	5.99	182.9	479	4.30	2.8	28.8	845	<0.0	<20	0.04	<2.0	1.813
Freda		11	6.29	232.1	672	2.12	2.24	30.1	1200	<0.0	<30	0.015	<2.0	1.895
Wedderburn		10	6.12	234.0	529	1.45	1.47	32.7	1190	<0.0		0.058	2.4	1.997
subgroup sHL (high-Au, low-Ni)														
Chebankol		19	5.16	91.7	108	22.8	52.5	18.4		0.3	<60	0.090		2.00
Lonaconing		29	5.35	96.9	168	24.8	62.1	22.6	194	0.37	99	0.746		2.22
Sombrerete	nc	44	5.07	98.4	247	19.9	11.3	21.1	213	2.04	<100	0.08		2.26
Hassi-Jekna		17	5.53	107.2	177	23.6	69.6	26.6	350	0.21	<20	0.231	1.5	2.40
Algoma		<20	5.48	105.1	264	20.1	38.3	25.9	<240	0.23	<80	0.354		2.45
Magnesia		23	5.32	107.0	247	14.2	22.4	23.2	270	0.21	<40	0.139		2.74
Qarat al Hanash		34	5.51	127.5	212	16.7	29.7	26.7	316	0.27	100	0.856		2.78
Victoria West		12	5.76	124.3	158	16.6	31.4	29.8	200	0.20	<30	0.032	2.7	2.93
Muzaffarpur		44	6.06	139.9	213	15.4	28.6	32.2	433	0.38	75	0.550		3.36
subgroup sHH (high Au, high Ni, includes Gay Gulch trio)														
Garden Head		8	6.18	171.6	409	10.8	16.6	22.9	279	0.15	<30	0.115	1.8	2.44
Gay Gulch		13	6.77	150.7	245	6.51	10.7	22.9	338	0.39	<20	0.099		2.55
Mount Magnet		10	6.05	145.7	195	7.67	5.26	24.7	400	<0.4	<60	0.015		2.64
Allan Hills ALHA80104		10	6.80	158.6	298	5.87	10.3	26.3	567	0.37	<30	0.083	4.2	2.63
Kofa		7	6.94	183.9	465	4.79	8.61	28.4	621	0.34	<20	0.1		2.85
Linville		11	6.13	165.1	278	7.84	16.1	30.0	590	<0.2	<120	0.01		3.04

(continued)

Table 2. (Continued)

Meteorite	sil[a]	Cr (μg/g)	Co (mg/g)	Ni (mg/g)	Cu (μg/g)	Ga (μg/g)	Ge (μg/g)	As (μg/g)	Sb (ng/g)	W (μg/g)	Re (ng/g)	Ir (μg/g)	Pt (μg/g)	Au (μg/g)
Udei Station grouplet, closely related to sLL														
Thiel Mountains	ac	209	4.70	80.4	174	73.6	234	12.7	429	1.02	245	3.67	6.2	1.529
Udei Station	ac	47	4.81	94.7	275	69.4	204	15.2	639	0.74	136	0.672	3.6	1.602
Caddo	ac	134	4.90	94.2	352	68.4	273	14.5	446	1.05	287	2.53	6.4	1.607
Harlowtown		21	4.91	87.5	331	60.6	222	16.5	396	0.63	238	2.65		1.608
Four Corners	ac	30	5.03	90.3	260	49.4	179	16.3	500	0.61	233	2.35	5.3	1.636
Zagora	ac	64	4.83	93.6	267	70.1	226	15.6	350	0.88	267	2.83	6.3	1.706
Pitts grouplet, intermediate between sLL and sLM														
Woodbine	ac	75	5.42	100.5	167	35.8	114	17.8	523	0.60	209	1.98	5.3	1.640
Colfax		17	5.23	107.4	326	53.1	153	17.9	533	0.51	147	1.78		1.656
Pitts	ac	14	5.60	128.1	376	34.5	95.6	20.2	911	0.33	95	1.22	1.8	1.700
Algarrabo duo														
Livingston (TN)		32	4.13	72.3	297	59.4	250	13.4	390	0.83	86	0.794	4.8	1.421
Algarrabo (Ovalle)		33	4.41	80.6	281	64.7	267	14.5	316	1.02	932	10	8.2	1.459
Mundrabilla duo														
Waterville		380	4.82	76.3	159	67.3	196	15.9	338	0.72	37	0.372	3.1	1.634
Mundrabilla	sr	241	4.95	75.0	125	58.3	196	15.4	394	0.55	91	0.906		1.643
Britstown duo														
Britstown		<15	5.51	190.6	1044	39.0	183	25.0	2090	0.61	2.45	2.10		1.927
Elephant Mor EET87506		38	5.40	208.3	1069	22.6	104	29.4	2670	0.36	279	3.06	6.7	1.982
NWA 468 duo														
Grove Mtns GRV98003		12	6.89	146.3	371	6.96	<50	21.8	404	0.60	<40	0.068	5.9	2.16
North West Afr	ac	230	7.19	118.5	263	31.0	117	22.8	431	0.65	281	2.75	4.0	2.21
Twin City duo														
Santa Catharina		9	6.17	358.8	1440	5.22	9.01	38.1	2760	0.20	<100	0.023		3.64
Twin City		<14	6.17	304.8	1140	4.53	7.50	37.6	2340	<0.2	<200	0.019		3.68
solo irons related to IAB														
Elephant Mor EET84300	ac	80	5.04	101.1	195	40.0	92.4	13.6	362	0.32	163	1.83	3.0	1.286
Kendall County	ac	211	3.95	55.5	450	74.4	347	10.8	721	1.01	270	2.11	9.3	1.397
Ellicott		18	4.91	78.5	175	60.0	252	13.6	190	1.50	304	3.46		1.400
Vermillion	nc	41	4.88	74.9	122	46.2	140	13.0	124	0.59	240	1.96	2.0	1.415
Yongning		37	3.96	64.4	151	93.9	490	10.3	350	2.08	389	3.97	11.2	1.450
Georgetown		290	4.79	90.3	358	56.0	120	16.2	393	0.63	<20	0.238	3.0	1.507
Mertzon		667	3.97	90.8	653	65.5	293	12.7	529	0.96	207	2.20		1.528
Oktibbeha County		23	4.77	596.3	6460	3.61	9.00	31.4	3785	0.40	<0.35	0.026		1.615
Aswan		18	5.92	82.0	122	20.8	41.8	16.6		1.66	<50	0.249	12.1	1.670
Wu-Chu-Mu-Chin		15	5.94	221.7	801	48.2	140	21.0	750	0.76	262	2.64	6.6	1.681
Cookeville		29	4.29	70.3	154	89.8	398	13.2	287	1.18	251	2.46	8.9	1.707
Burkhala		65	4.73	97.2	461	54.0	358	12.3	637	1.60	759	8.03	12.4	1.711
Mesa Verde Park		18	4.88	108.3	325	55.2	142	16.6	469	0.54	297	2.16	4.9	1.800
San Cristobal	pb	17	6.13	252	944	11.5	24.3	29.4	2155	<0.2	<40	0.329	2.3	1.999
Ventura		15	6.32	101.4	149	13.9	25.0	21.8	119	0.87	24	0.163	6.7	2.14
Lime Creek		<30	6.00	292.9	1109	15.7	28.6	43.8	2630	<0.3	<280	1.05		2.28
Quesa		17	6.66	119.7	211	36.8	100.6	27.5	221	0.69	<60	0.092		2.92
IAB related? Au values below the range plotted														
Zacatecas 1792		155	4.80	59.9	123	80.8	307	6.8	<100	1.91	130	2.14	11.6	0.744
Northwest Afr NWA176	ac	430	4.14	86.0	300	18.7	197	9.42	100	1.16	355	3.62	8.5	0.862
Bocaiuva	ac	161	4.14	84.8	290	19.1	1.78	9.83	200	1.20	363	3.19	6.3	0.879

[a] Silicate textures are largely from Benedix et al. (2000.
Texture abbreviations: ac, angular chondritic; gr, graphite-rich; nc, nonchondritic; pb, phosphate-bearing; sr, sulfide-rich.
[b] Two mean analyses (high- and low-Ir) given for Canyon Diablo.

mainly use the shorter form sLH when the context is clear. The two grouplets consist of meteorites closely related to the low-Au groups.

In Figure 2 we repeat the Ni-Au diagram (Fig. 2a) and also include three diagrams that rank next to Ni-Au in potential for classifying the extended IAB set: Co-Au, As-Au, and Ga-Au. In Figure 3 we show data for four additional taxonomically valuable elements; the Ge-Au diagram is almost as good as the first four diagrams, and the Sb-Au and W-Au results are quite useful when high-precision data are available. The Cu-Au diagram is good but, as discussed below, Cu values may show sampling variations that limit their utility. The main group and the five subgroups are shown on these diagrams by different filled symbols, except sLL by Xs. One of the low-Au grouplets is shown by crosses, the other by open triangles.

Filled triangles are used for five pairs of irons that are related to greater or lesser degrees. A large set of 17 irons that fall close to one or the other group on some diagrams but not on others, and are therefore not assigned to any group, are plotted as open squares. These are also not closely linked to each other in composition. Nonetheless, all have compositional characteristics suggesting genetic links to IAB.

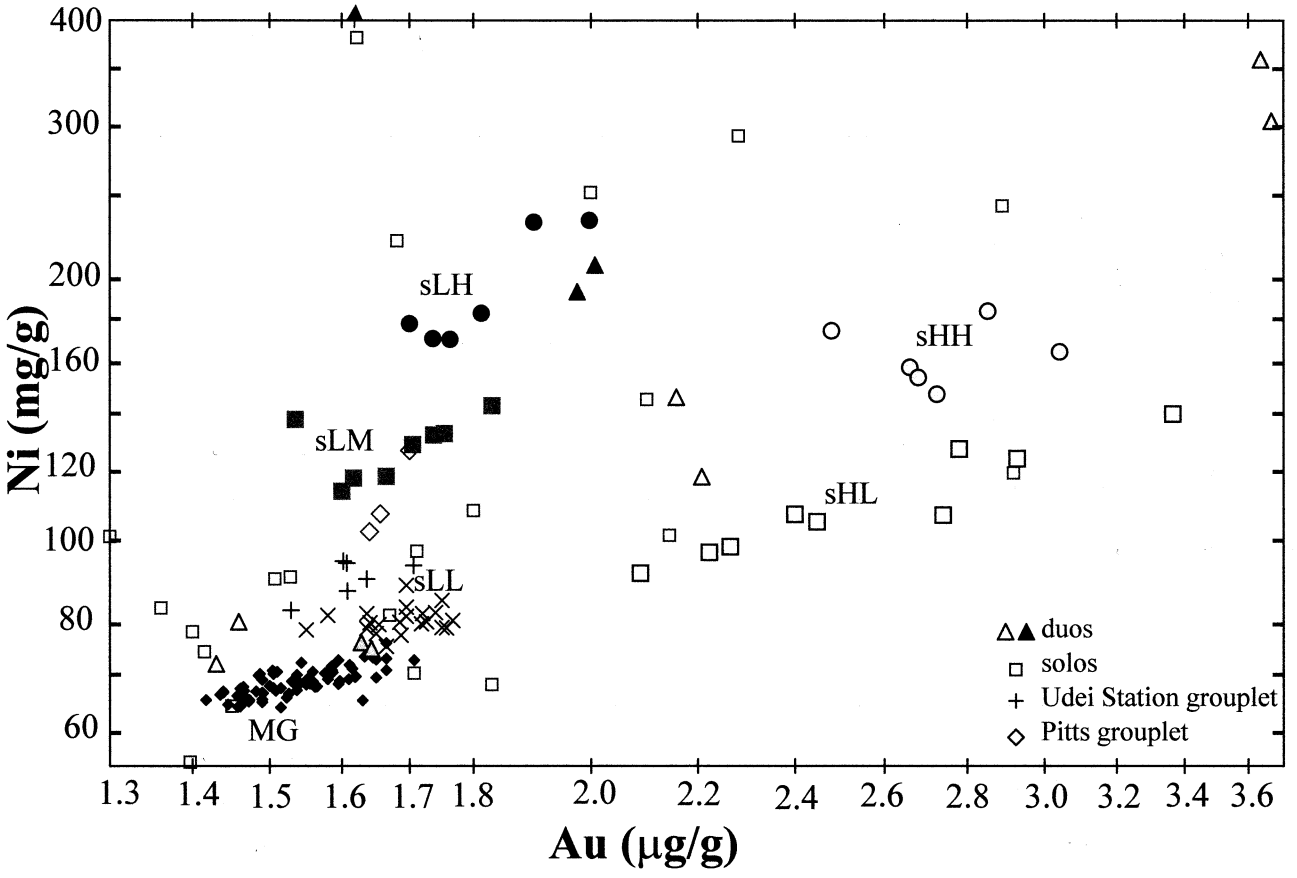

Fig. 1. This plot of log Ni vs. log Au shows the resolution of iron meteorites in the IAB complex into a main group (MG), five subgroups, five duos (filled triangles, pairs of compositionally closely related irons), and 17 solos (open squares, irons that are not closely related to any other iron). The main group (ca. 70 irons) forms a dense band; the subgroups form more diffuse fields that are roughly parallel to the main-group trend. The subgroups are given two-letter names, the first letter being L or H for high or low Au, and the second letter being H, M, or L for high, medium, or low Ni. The sLH group (dark filled circles above the main group) largely consists of the old IIID irons, and the sLM subgroup (dark filled squares between the MG and sLH) is largely comprised of the old IIIC irons. The three low-Au subgroups are closely related to the main group; many of these irons have coarse silicate inclusions with chondritic compositions and $\Delta^{17}O$ values near $-0.5‰$.

On the Ni-Au diagram (Fig. 2a) we see that with the exception of one high-Au MG iron that overlaps sLL, the MG field (small filled diamonds) is completely resolved from irons in the five subgroups. The subgroups show similar, subparallel trends on the Ni-Au plot, and (with the mentioned exception) are separated from the main group and each other by hiatus. Cases like this, where hiatus are present, provide convincing evidence that we are dealing with sets of meteorites that had different origins, and thus must be assigned to different groups or subgroups.

The Co-Au diagram (Fig. 2b) shows strong evidence for the same compositional clusters. There is appreciable overlap between the main group and the sLL subgroup but otherwise all groups are resolved. The total range in main-group Co contents is from 4.4 to 5.1 mg/g; the fact that this main-group cluster is so compact is a testimony to our high precision for Co. The spread in Co within any narrow range in Au is only about $\pm 3\%$ around the mean. Particularly striking are the parallel trends in the main group and the sLH and sLM subgroups.

The combination of fractional crystallization and mixing effects that determines the compositions of the irons in magmatic groups produce similar fractionations in As and Au; As-Au plots of these groups yield linear trends having similar slopes and, generally, similar intercepts (Wasson and Richardson, 2001). Nevertheless, we found that the As-Au diagram (Fig. 2c) had good taxonomic value for resolving irons in the IAB complex. Although there is more overlap between groups than on the Ni-Au diagram, only sLL shows appreciable overlap with the main group. As on the other diagrams, the main-group field is quite linear and compact. Similar to the Co-Au diagram, As-Au trends through the low-Au subgroups seem to be subparallel to those in the main group but slightly higher than predicted by an extrapolation of that trend.

In contrast to the positive trends in Figures 1a–1c, the Ga-Au diagram (Fig. 2d) shows negative trends in the main group and the subgroups. Again, the main-group field is dense, essentially linear, and sharply defined. Overlaps are only observed between the main group and sLL. Note that (in part because of low-Ga irons being assigned to sLL) the total range in main-group Ga is from 101 to 68 μg/g. In the past (Choi et al., 1995) the lower limit of the IAB Ga range extended down to 11 μg/g in San Cristobal but our improved and enlarged data set shows

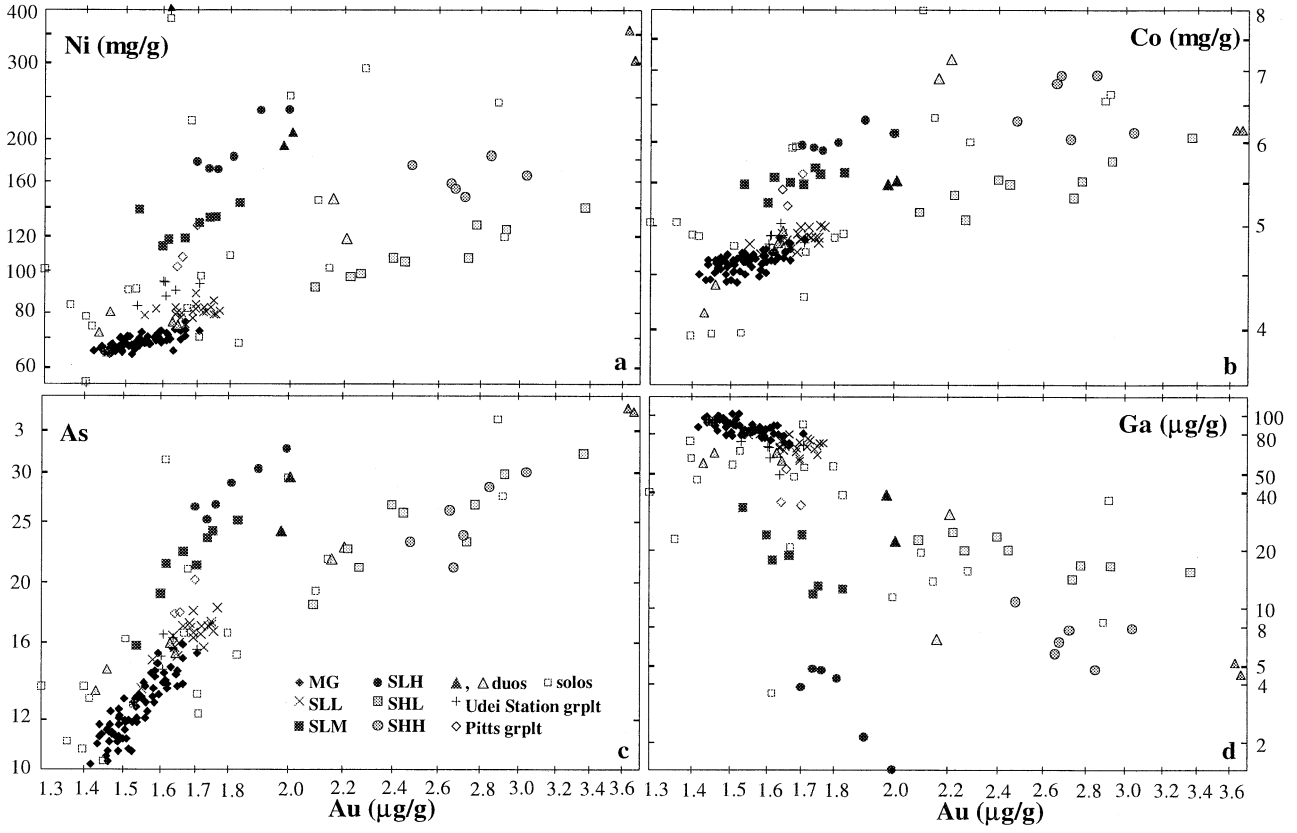

Fig. 2. Element-Au diagrams resolve the iron meteorites that meet our compositional criteria into the IAB main group, five subgroups, two grouplets, five duos, and 17 solos. See Figure 1 for the identification of the fields and symbols. Here we show the four most-useful element-Au diagrams for classification: (a) Ni, (b) Co, (c) As, and (d) Ga. On each of these the main group forms a well-defined linear band. On the Ni-Au diagram five subgroups are resolved from the main group and from each other; the trends in the subgroups are roughly parallel to those in the main group. The five groups are also resolved on the Co-Au, As-Au, and Ga-Au diagrams with the exception of the partially overlapping main group and sLL subgroup. The trends in all groups are negative on the Ga-Au diagram, positive on the other three diagrams. The low-Au and high-Au (sub)groups are discussed separately.

that this iron is not closely related to the main group (or to any other iron in the IAB complex).

In the four diagrams in Figure 3 the same general patterns are present but they are less well defined. The main-group Ge-Au trend (Fig. 3a) is negative, similar to that observed for Ga-Au. There is again overlap of sLL with the high-Au part of the main-group trend. The main-group W-Au trend (Fig. 3b) is also negative; the relationship between the main group and the sLL subgroup is similar to those on the Ga-Au and Ge-Au diagrams but there is more scatter. Although a part of this scatter is the result of the relatively high experimental uncertainties in our W data, a part may also reflect fractional crystallization effects discussed later in connection with our Ir results. Because of our relatively high detection limit, we are only able to report one W value for sLH, which (as shown by the Ir data) has low contents of refractory siderophiles and those volatile in oxidizing environments (e.g., Ga and Ge).

As shown in Figures 2c and 2d, the main-group Cu-Au and Sb-Au trends are positive; in both diagrams a compact core region resembles the element-Au trends for Ni, Co, and As, but there are substantially more outliers. Our Sb errors are relatively large, and most of the outliers may reflect either experimental errors or, for some high values, contamination before receipt in our laboratory. Although Cu is a valuable taxonomic parameter for the magmatic irons, in the IAB complex there is more scatter, some of which we attribute to effects associated with the presence or absence of metallic Cu in the system.

All the elements we determine are concentrated in the Fe-Ni phases kamacite and taenite with the exception of Cr and Cu. There is no doubt that much of the Cr is in chromite. Metallic Cu grains are found in IAB irons, mainly associated with graphite-FeS nodules (El Goresy, 1965; Kracher et al., 1975). Our Cu replicates for Landes and Lueders scatter; these need to be restudied. However, as discussed below, most anomalously high Cu values replicated very well.

We suggest that Cu values are lower in irons that were able to nucleate metallic Cu at relatively high temperatures, with this step followed by the diffusional drain of the Cu out of the Fe-Ni into the Cu metal. In ordinary chondrites, metallic Cu tends to nucleate at the boundaries between metal and FeS (Rubin, 1994). The observed " normal" main group level of ca. 150 μg/g Cu might then reflect the equilibrium Cu content of the Fe-Ni at the diffusional blocking temperature.

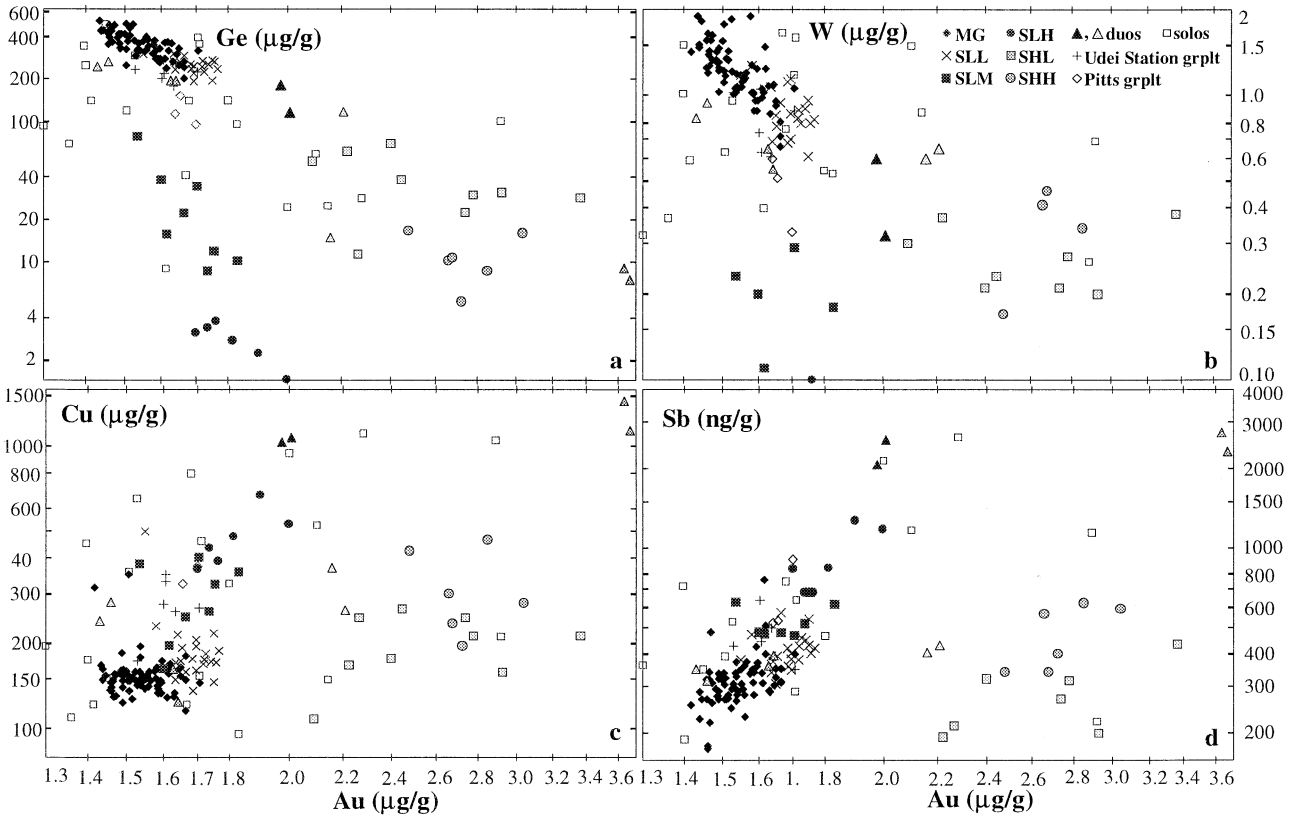

Fig. 3. Four other element-Au diagrams have taxonomic value. The (a) Ge-Au diagram offers about the same resolution as the Co, As, and Ga-Au diagrams on Figure 2. The other diagrams show more scatter, which limits their usefulness, but the scatter fields are consistent with those on the Ge-Au diagram and those seen in Figure 2. The Ge- and W-Au trends are negative, similar to the Ga-Au trend. The Cu-Au and Sb-Au trends are positive in the main group, but the slopes are low and the trends only marginally resolvable because of the scatter in the data. On all diagrams in Figure 2 and in three of the diagrams in Figure 3 the sHL subgroup (large gray squares) plots along a rough extrapolation of the main-group trends, but the sHL Sb data appear to be resolvably lower than such an extrapolation.

3.3. Assignment of Meteorites to Subgroups

3.3.1. Low-Au subgroups and grouplets

The main-group fields are well defined in Figures 2a–2d and Figure 3a (Ge-Au). We suggest that, by comparing the data distributions in the main group with those in other clusters that appear on these diagrams, we can assess whether members of such clusters are sufficiently related to warrant (sub)group status. It seems clear that sLH and sLM (the old groups IIID and IIIC, respectively) have properties consistent with assignment to a group. If their compositional links to the main group and to each other were not so close, we would treat them as independent groups, as worthy of this status as other small groups of iron meteorites (such as IIC or IIIF).

The new sLL subgroup is also well defined on the Ni-Au diagram, occupying a position between the main group and the sLM subgroup but nearer the main group. Its existence as a satellite of the main group is one of the reasons for holding that the sLH and sLM subgroups should be treated as part of the same complex. As discussed below, on most other diagrams sLL shows appreciable overlap with the main group but it is somewhat resolved on the As-Au, Co-Au, and Cu-Au diagrams. Among the low-Au groups, sLL is the only one whose existence had not previously been proposed.

In addition to the sLH, sLM, and sLL subgroups there are two low-Au grouplets that are closely related to the main group. We named these after one of their members that is an observed fall. On the Ni-Au diagram these grouplets occupy the region between sLL and sLM. The “Udei-Station” grouplet has lower Ni contents; it has six members (enough to be called a group but we suggest it needs better definition before this designation be given), four of which contain coarse silicate inclusions. The “Pitts” grouplet has higher Ni contents; two of its three members contain coarse silicates. Although we are dealing with the statistics of small numbers, it is noteworthy that neither the main group nor any of the other subgroups has such a high fraction of coarse-silicate-rich members as these two grouplets.

Subgroup sLL generally appears to form a high-Au extension of the main group. On the Co-Au (Fig. 2b), As-Au (Fig. 2c), and Cu-Au (Fig. 3c) diagrams most values plot slightly higher than the (positive) main-group trend. In each of these cases the mean element/Au ratios are significantly higher in sLL than in the main group. The other diagrams that provide the best resolution of the low-Au subgroups are Co-Au, Ga-Au, and Ge-Au (Figs. 2b, 2d and 3a); on these diagrams sLH and

sLM are fully resolved from each other and from other groups. This is also marginally true on the As-Au diagram, Figure 2c. On all these diagrams sLL partially overlaps the main group. On the W-Au diagram (Fig. 3b) subgroups sLH and sLM are resolved from each other and from all other groups, but our detection limit only permitted us to report one value for sLM. Subgroup sLL overlaps the main group.

3.3.2. High-Au subgroups

The two high-Au subgroups are designated sHH (high Au, high Ni) and sHL (high Au, low Ni). Included in the former is the previously recognized Garden-Head trio/quartet (Malvin et al., 1984; Kracher et al., 1980). The sHL subgroup is new; it consists of eight irons that, on most diagrams, form an array that could plausibly be interpreted as an extension of the main group to higher Au contents. These two high-Au subgroups are less well defined than the low-Au subgroups. In each of them there are possible reasons to discard one or more irons from the set. Because of these complexities we need to gather more chemical and textural observations; we therefore reserve the detailed discussion of them for a subsequent paper.

Malvin et al. (1984) had noted the general compositional relatedness among several of the high-Au meteorites (including the Garden-Head quartet) that are now assigned to these high-Au subgroups, and speculated that they might be related to the IIIC and IIID irons. However, at that time the compositional evidence was not precise enough to warrant assigning the irons we now designate sHL to a single group.

Because the two high-Au subgroups are fully resolved from the main group and the three low-Au subgroups in terms of Au, we will not compare them to these groups. Instead we will confine our discussion to two topics: (a) are the compositional data fully consistent with these two sets of irons being designated groups? and (b) are the two sets of irons properly resolved from each other?

The two high-Au subgroups are fully resolved from each other on the Ni-Au (Fig. 2a), Ga-Au (Fig. 2d), and Co-Au (Fig. 2b) diagrams, but only marginally on the latter. In fact, the vertical spread in Co in sHH, which is much larger than that observed in the main group, calls into question the assignment of group status to this set of five irons. The groups are also resolved on the Ge-Au diagram (Fig. 3a), with the exception of sHL Sombrerete (2.26 μg/g Au), which is inside the sHH range, $\sim 4\times$ lower than expected from the trend through the remaining irons assigned to sHL. On the As-Au diagram the two groups are fully intermingled.

We noted above that the sHL data plot along rough extrapolations of the main group on most diagrams. The exception is the Sb-Au diagram (Fig. 3d). Here the generally upward trend of the main group would seem to extrapolate well above sHL. Unfortunately, this conclusion is tempered by the large degree of scatter among our main-group Sb data (in part because of a moderately high analytical uncertainty).

Our conclusion is that both of these high-Au groups include irons that are closely related, but also that there may be interlopers in each group. The logical next step is to make a detailed comparison of their structures, and to gather additional O-isotope data, perhaps using laser-fluorination to study individual silicate grains (Young et al., 1998).

3.4. Silicate Inclusions in the Irons of the IAB Complex

It is useful to review the basic evidence regarding silicates in the IAB-complex irons because these provide additional information regarding the classification and the origin of these irons. The silicates can either be coarse (grains or aggregates >2 mm) or fine and dispersed. Those with coarse silicates are identified in Table 2.

It appears that fine silicates are ubiquitous in the irons originally assigned to IAB-IIICD, i.e., in the main group and the closely related low-Au subgroups and grouplets. El Goresy (1965) found silicates in every graphite-troilite inclusion he examined in the IAB irons Canyon Diablo, Odessa, and Toluca (but did not find them in graphite-free FeS inclusions). In Appendix I of Buchwald (1975), silicates are reported in 69 irons listed under the old name of IAB, group I. From this list we deleted Thoreau (paired with Odessa) and four irons (Pan de Azucar, Mayerthorpe, Surprise Springs, and Petropavlovsk) for which Buchwald's samples were so small that he failed to find troilite, cohenite, or graphite in this inclusion-rich group. These corrections lead to a calculated silicate-bearing fraction of 42%. Because the tiniest silicates are easily missed, this must be interpreted as a lower limit.

A sizable fraction of the irons contain coarse silicates, big enough to allow textural studies and, in favorable cases, to use modal abundances to estimate bulk compositions. Benedix et al. (2000) studied four of these occurrences and summarized the results of earlier studies on 19 others (they also included Tacubaya but we agree with Buchwald (1975) that this Mexican iron is probably paired with Toluca). They divided these silicate assemblages into five categories: angular chondritic (ac), nonchondritic (n), sulfide-rich (sr), rounded, graphite-rich (rg), and phosphate-bearing (pb); in six cases they report two of these categories in a single iron. Chondritic silicates dominate, and are reported in 19 of the 23 irons on their list (if Tacubaya, which has chondritic silicates, is indeed Toluca). We list their classifications in column 2 of Table 2. In part because we also include the so-called IIICD and ungrouped IAB-related irons, our list includes five other occurrences in which silicates with dimensions >2 mm are known among the members of the complex.

In Figure 4 the compositions of the irons that contain coarse silicates are shown on the Ni-Au diagram. With four exceptions, all reported oxygen-isotopic compositions in the silicates fall within a narrow range; $\Delta^{17}O$ ($= \delta^{17}O - 0.52\cdot\delta^{18}O$) values summarized by Benedix et al. (2000) are all between -0.30 and -0.68‰. This is within (towards the upper end of) the range for whole-rock carbonaceous chondrites and suggests that the precursor materials were carbonaceous chondrites. Circles are drawn around the symbols of irons that contain silicates having this classic IAB O-isotope composition, diamonds around the four that have more negative $\Delta^{17}O$ values.

The diagram shows that three of the latter four irons have Au > 2 μg/g. The exception at Au 1.42 is Vermillion; its $\Delta^{17}O$ is -0.76‰, not fully resolved from that of Lueders at -0.68‰. The other three meteorites have more negative $\Delta^{17}O$ values, even deeper within the carbonaceous chondrite O-isotope range: Sombrerete (– 1.39‰; tentatively assigned to the sHL; Clayton and Mayeda, 1996), NWA468 (-1.39‰; a member of the NWA468 duo; Rubin et al., 2001); and Yamato 8451 (-0.77‰, solo ungrouped, Clayton and Mayeda, 1996).

All except one of the irons having classic O-isotopic compositions form a diagonal band extending from Kendall County on the

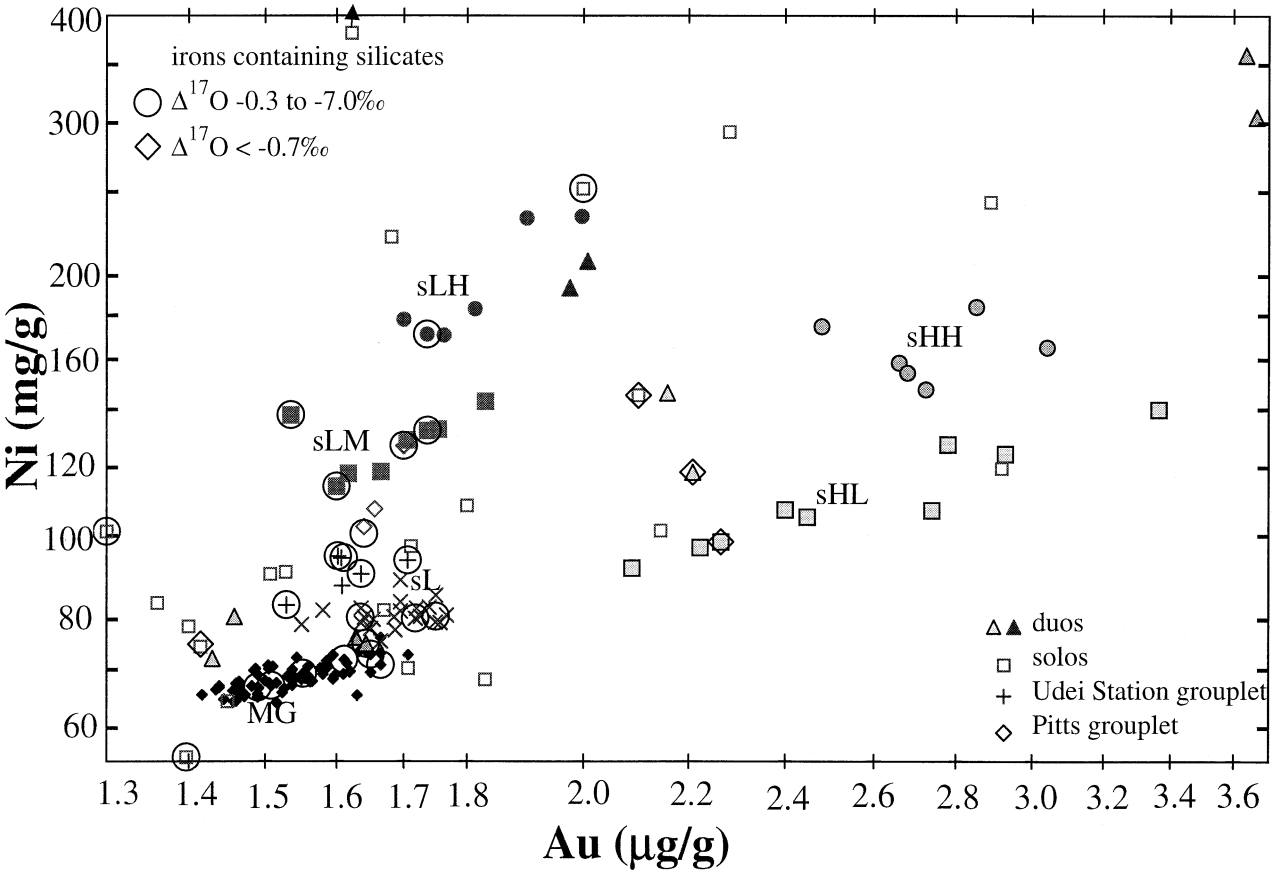

Fig. 4. This plot of log Ni vs. log Au shows the positions of the irons from the IAB complex that contain massive silicates. Circles around the points indicate that the $\Delta^{17}O$ of the silicates is in the classic range: $-0.30 \leq \Delta^{17}O \leq -0.68‰$; diamond outlines indicate the points having $\Delta^{17}O < -0.7‰$. With the exception of EET84300 on the left axis, the irons containing classic O-isotope compositions form a diagonal band extending from Kendall County on the bottom axis to San Cristobal at Au = 2.0 μg/g. Three of the other silicate-bearing irons have Au contents >2 μg/g. The other, Vermillion ($\Delta^{17}O = -0.76‰$) is just to the low-Au side of the lower end of the main group.

lower left (Au 1.4 μg/g) and to San Cristobal on the upper right (Au 2.0 μg/g). The lone exception, at Au 1.30 μg/g is EET84300.

The silicates in the main group and the low-Au subgroups and grouplets are reduced. The highest olivine Fa content is 8.0 mol.% in Udei Station (assigned by us to the Udei Station grouplet). The most reduced olivine is Fa1.0 in Pine River (Benedix et al., 2000), a member of the sLL subgroup. A still lower value (Fa0.8) is present in the olivine of Elephant Moraine EET84300, but the Au content (1.31 μg/g) of this ungrouped iron is slightly below the IAB range (but near an extrapolation of sLM to low Au values). Because its O-isotope composition is similar to that of low-Au members of the complex ($\Delta^{17}O = -0.50\%$; Clayton and Mayeda, 1996), it should probably be included in discussions of members of the IAB complex.

In these silicates the olivine Fa content is lower than the low-Ca pyroxene Fs content. As discussed by Kallemeyn and Wasson (1985), equilibrium between these phases leads to the opposite trend. Thus, Fs > Fa indicates that reduction was ongoing as temperatures fell. Diffusion rates are appreciably lower in pyroxene than olivine, thus the pyroxene preserves an earlier, more oxidized state. It follows that the original precursor chondritic materials had higher mean olivine Fa and low-Ca pyroxene Fs values. The graphite and carbides common in these meteorites could have served as reducing agents providing the resulting CO was able to escape (Kracher, 1985). This discussion leads to a key question regarding the origin of IAB: what were the original FeO/(FeO + MgO) ratios in the silicate precursors? It would be most useful to examine whether the detailed compositions of the silicates vary systematically among the groups, subgroups, and grouplets.

In our set of meteorites the only silicates that are known to be FeO-rich are found in Sombrerete, a possible member of the sHL subgroup. According to Prinz et al. (1983), these globular silicates mainly consist of plagioclase and glass together with minor (modal 15%) $Fs_{25}Wo_{05}$ orthopyroxene. Thus, these are not chondritic, but similar to the impact melts observed in IIE irons that are closely related to H chondrites. However, the low $\Delta^{17}O$ value of Sombrerete clearly indicates an affinity to carbonaceous chondrites.

3.5. Some Properties of the Subgroups

Subgroup sLL overlaps the main group on most diagrams, and the members are clearly closely related to the main-group irons. One property that can immediately be noted in Table 2 is

that several of the members of this subgroup contain coarse silicates.

One sLL member, Annaheim, has an exceptionally high (500 μg/g) and reproducible Cu content. Values in the remainder range from 230 in Karee Kloof down to 150 in Bahjoi and Ogallala. As discussed above, a possible way to produce scatter in Cu values that were initially more uniform is to nucleate a Cu-rich phase such as Cu metal followed by diffusive draining of Cu out of the Fe-Ni metal.

Subgroup sLM includes all the meteorites originally assigned to IIIC by Wasson and Schaudy (1971). These have now been augmented by Egvekinot and the silicate-rich iron Maltahöhe (McCoy et al., 1993). Coarse silicates are abundant in Persimmon Creek which, because its Ni content is 25 mg/g higher than expected from the sLM trend (see Fig. 2a), we designate it an anomalous member of the group; on some diagrams (Ni, Cu, Sb) Persimmon Creek could be assigned to sLH. The only other sLM containing coarse silicates is Carlton (Kracher and Kurat, 1977) and even here they are sparse.

Subgroup sLH includes all the meteorites assigned to group IIID by Wasson and Schaudy (1971). The only member of this small group to contain coarse silicates is Dayton; these rare assemblages were first reported by Fuchs et al. (1967) and more completely characterized by Prinz et al. (1982).

3.6. Other Meteorites Associated with the IAB Complex

There are many ungrouped irons that show compositional links to group IAB. It was therefore necessary to establish criteria for relatedness to the IAB complex. Initially we mainly chose irons having high Au and As values and other features similar to those common in the high-Ga (>50 μg/g) IAB irons. Then, after working our way through the data sets for the main group and the five subgroups, we chose the following compositional threshold values for possible membership in the IAB complex: Au >1.3 μg/g, As >10 μg/g, Co >3.9 mg/g, Sb >180 ng/g, and $0.4 \leq Ge/Ga \leq 7$. Some meteorites were included even though we had no Sb data; we inferred that these meteorites belong to the IAB complex based on concentration data for other elements (or, for the main group, from textural observations). The criterion based on the Ge/Ga ratio eliminates some meteorites (Dehesa, Soroti, Yamato Y75031) that are otherwise compositionally similar to IAB-complex irons. Because Ge and Ga tend to fractionate so coherently, we felt that this criterion was useful, but it is possible that future studies will show that these deserve inclusion in the IAB complex.

In addition to the meteorites assigned to the main group and the five subgroups, we show data on Figs. 2 and 3 for five duos (pairs of more-or-less related irons) and 17 solos that, on the basis of these criteria, appear to be members of the IAB complex. The data for the duos are plotted as filled triangles that are obviously related on most diagrams. The solos are shown as open squares.

In some diagrams these ungrouped irons may plot within the field of one of the groups or along an extrapolation of a group trend. In Appendix A we briefly discuss each of these cases and discuss the compositional data that convinced us that these irons should not be assigned to one or the other groups. The compositional evidence nonetheless supports the view that the ungrouped irons listed in Tables 1 and 2 have properties consistent with assignment to the broad IAB complex, and that most if not all formed by the same processes that produced the members of the groups.

4. TRAPPED MELT AND NONMETALS IN IAB

4.1. Evidence of Trapped FeS-rich Melt in Irons in the IAB Complex

Most IAB irons contain moderately large (1- to 5-cm) ellipsoidal troilite nodules. These contain variable amounts of graphite; for example, Buchwald (1975) observed a graphite fraction of 0 to 50 vol.% in the nodules of Gladstone (iron). We refer to these objects as troilite nodules even though the graphite fraction can be large. The troilite nodules are surrounded by shells of cohenite and schreibersite >1 mm thick. They also contain minor phases including silicates and chromite.

The solubility of S is very low in metallic Fe-Ni; $D_S < 0.01$. If we assume that $D_S = 0.005$ and that typical S contents of IAB melts were 200 mg/g or less, we calculate a maximum content of S initially dissolved in the solid metal of 1 mg/g. In Table 3 we list the S contents estimated for IAB irons by Buchwald (1975), including seven meteorites that belong to the main group. Buchwald also listed a value for MG Burkett, but closer examination showed that this low value (1.7 mg/g) is based on a bulk chemical analysis; because it seems unlikely that the analytical sample included a representative amount of FeS inclusions, we rejected it. His high S value for MG Bogou, 20 mg/g, is based on an area of only 83 cm^2; we list it but do not include it in the IAB mean. All values are >4 mg/g. We also list an estimated S content obtained by R. S. Clarke (personal communication, 2001) for the United States National Museum (USNM) El Taco slice of MG Campo del Cielo.

Buchwald also provided S values for what he called group-I-Anom meteorites and for some other IAB-related irons such as Mundrabilla and Waterville. One I-Anom iron, Bendego, is now assigned to group IC and not closely related to IAB; the other four are listed in Table 3. Of these, only Persimmon Creek is assigned to one of the subgroups; as noted above, it is a compositionally anomalous member of sLM. Pitts is a member of the closely related Pitts grouplet.

In magmatic group IIIAB melt seems to have been trapped by stochastic mechanical events such as the collapse of the core (or core-mantle) structure (Wasson, 1999). However, the relative uniformity of the FeS distribution in most IAB irons suggests that they were trapped as a result of the rapid solidification of the melt.

The moderately high abundances of FeS obtained by modal integration (Table 3) suggest that most IAB irons include large melt fractions. If we knew the S content, we could use these values to obtain the melt fraction. In terrestrial layered intrusions the composition of the parental melt is estimated from the chill zone at the edge of the magma chamber. Here, unfortunately, we do not have field relationships that allow the unambiguous recognition of such chill zones. Nevertheless, there is reason to believe that we have some chill zones, particularly in the silicate-rich members of the IAB complex. For example, the section of Pitts illustrated in Buchwald (1975) shows many features that could reflect quenching of an FeS-rich melt mixed with abundant silicates. The structure of Persimmon Creek, which we designate an anomalous member of the sLM subgroup, is similar.

Our modal analysis of a photo of the Pitts section yielded a

Table 3. IAB irons for which Buchwald (1975) reported S contents.

Meteorite	Au (μg/g)	Ni (mg/g)	C (mg/g)	P (mg/g)	S (mg/g)	area (cm^2)
Main group						
Bogou[a]	1.65	73.3	—	1.7	20	83
Campo del Cielo	1.49	66.8	—	2.5	4[b]	4000
Canyon Diablo	1.53	69.3	10	2.6	10	1620
Gladstone (iron)	1.49	65.6	—	2.7	11	900
Odessa (iron)	1.61	71.9	2	2.5	5	500?
Toluca	1.72	80.2	—	1.6	7	3100
Wichita County	1.56	67.9	—	2.0	12	348
Youndegin	1.54	68.3	6.4	2.5	4.3	204
Other than main group						
Mertzon	1.53	90.8	—	2.5	14	80
Mundrabilla	1.64	75.0	10	2.6	80	>1000?
Persimmon Creek	1.54	141.7	—	2.0	30[b]	≈30?
Pitts	1.70	127.1	—	2.0	97[b]	24
San Cristobal	2.00	242	—	1.8	40[c]	>160?
Waterville	1.63	76.3	5	3.0	30	80

[a] Bogou data based on small (80-cm^2) section; not included in MG mean.
[b] The S contents of Campo del Cielo, Pitts, and Persimmon Creek are for the silicate-free fraction. The listed Campo del Cielo S value is a rough estimate made by R. S. Clarke for the large USNM El Taco slice; the Pitts S value is our estimate; Buchwald (1975) gives a lower value of 60 mg/g.
[c] Buchwald (1975) gives 40 mg/g S in the San Cristobal text, but 30 mg/g in his Table 30.

S content of 97 mg/g in the combined metal-FeS portion of this small (27-cm^2) section (USNM 1378). Although the uncertainty is high because of the small area of the section, this provides a rough estimate of the S content of one IAB melt. The main-group data summarized in Table 3 suggest that the S content of the main MG melt was several times smaller.

At the other extreme from Pitts is the large (5600 cm^2) El Taco slice of Campo del Cielo at the Smithsonian Institution (Fig. 78 in Buchwald, 1975). Despite the large abundance (4 vol.%) of coarse silicate inclusions, the maximum S content of this specimen is only ~1 vol.% FeS, equivalent to ~4 mg/g S (R.S. Clarke, personal communication, 2001). The relatively high Ga, Ge, and Ir and low Au and Ni contents of El Taco are also consistent with a low melt fraction.

4.2. The Nonmetal Composition of IAB Melts

Buchwald also estimated P contents for essentially all irons; we list in Table 3 his values for the irons in which he estimated S. Estimates of the contents of the less abundant nonmetals are most easily obtained from the irons having the highest S contents and thus the highest melt fractions. From the values tabulated for high-S MG irons in Table 3 we estimate a S/P ratio of roughly 5 g/g, similar to estimates for the magmatic groups (Wasson, 1999). The S/P ratio tends to be higher, ≈10 g/g, in the IAB-related irons.

The C content of IAB irons can be quite high. Buchwald (1975) lists a few values obtained by modal integration, and we have tabulated these in Table 3. His three MG C values range from 2 mg/g in Odessa to 10 mg/g in Canyon Diablo. Moore et al. (1969) and Lewis and Moore (1971) used a milling technique to obtain reasonably representative sampling of minor phases (including carbides). The highest C concentrations they observed are in the IAB irons Dungannon (4.55 mg/g—Lewis and Moore, 1971) and Rifle (1.8 mg/g—Moore et al., 1969). The mean of all their IAB values is lower, 0.80 mg/g. We suspect that, despite the milling technique, these authors did not adequately sample the C associated with large FeS nodules, and we suggest that the mean initial C content of main-group metal was ≥2 mg/g and that the C/Fe ratio was ≥0.01. Buchwald's modal integrations are too sparse to allow strong conclusions, but they suggest a mean C content in MG irons around 4 to 5 mg/g, similar to the Lewis-Moore Dungannon value.

5. FRACTIONATION OF IAB METAL BY CRYSTAL SEGREGATION, NOT FRACTIONAL CRYSTALLIZATION

5.1. Main-group Trends as Indicators of the Style of Fractionation

Our results show that most element-Au main-group fields are compact and also that the fields in the three closely related low-Au subgroups are reasonably compact (for the elements plotted on Fig. 2) and have trends similar in slope to those in the main group. Mainly because the data sets are smaller, there is generally more scatter in the fields of the subgroups than in the main group. The similarities in the properties of these element-Au fields offer important new constraints on possible models for the formation of the IAB groups.

As discussed above, the membership (and, thus, properties) of the high-Au subgroups are less well defined than the low-Au subgroups. Although we think it probable that these also formed by the same processes as the main group, we suspect that additional data will show that some of the listed members of the high-Au sets are outliers, and we therefore do not attempt to discuss their formation in the same detail that we devote to the main group and the low-Au subgroups.

5.2. The Fractionation of Ir in the IAB Complex

Past arguments for attributing a nonmagmatic origin to IAB included the small range in Ir and the low slope on Ir-Ni diagrams (Wasson, 1972; Wasson et al., 1980), and these are

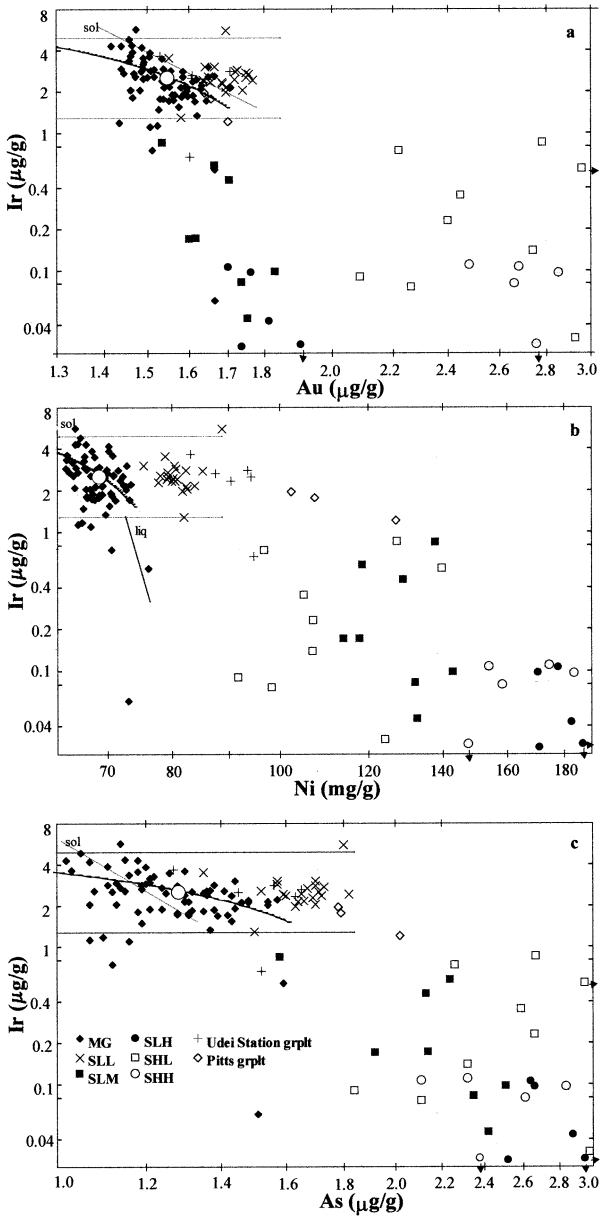

Fig. 5. Our Ir data are plotted on (a) Ir-Au, (b) Ir-As, and (c) Ir-Ni diagrams. With the exception of seven irons the Ir contents of main-group irons fall between 4.86 and 1.35 mg/g; horizontal lines mark these limits. On each of the diagrams there is a weak downward trend accompanied by considerable scatter (much larger than experimental error including sampling). Mean compositions are shown by circles, and estimated liquid-solid mixing curves are passed through these. Straight lines starting on the upper left of the main group on each diagram show how solid IIIAB tracks compare in slope. A IIIAB liquid track line is shown only for Ir-Ni; those for Ir-Au and Ir-As are above the upper Au and As limits of these diagrams.

still important arguments. In Figure 5 we show the data for the IAB main group and the five subgroups and the three grouplets on Ir-Au, Ir-As, and Ir-Ni diagrams. For clarity, the ungrouped irons are not plotted. Thin horizontal lines show the upper and lower limits of the Ir values that we included in this main discussion of a fractionation model. In section 6.5 we suggest that the values outside these limits show the effects of fractional crystallization, and should be excluded from the following discussion of a crystal-segregation model.

There is too much scatter on the three diagrams in Figure 5 to justify an exact determination of the slopes. We show two sets of lines on each diagram; the curve through the data is a rough fit generated by mixing equilibrium solid and liquids. The straight lines are IIIAB solid and liquid evolutionary tracks, based on Wasson (1999) and unpublished fits to the IIIAB Ni-Au data, and modified here to produce an initial solid having the composition 63.0 mg/g Ni, 10.1 mg/g As, 6.0 mg/g Ir, and 1.39 mg/g Au. The bottom ends of the solid tracks are truncated at an Ir content of 1.4 mg/g.

If we first focus on the Ir-Au diagram (Fig. 5a), we see that, with the exception of seven outliers having Ir contents outside the dense main-group cluster (demarcated by the thin horizontal lines), the total range in Ir is only a factor of 3.6 (from 4.86 to 1.35 mg/g). There is a downward trend, which we have roughly fit with a mixing-curve. If one were to exclude the five main-group members having the highest Au contents, the mixing-curve slope could be increased by a factor of 2. If, in contrast, we have mistakenly separated the sLL subgroup from the main group, the slope estimate would be smaller. If we were to claim that sLH and sLM members formed in the same fractionation process, we would again obtain a steeper slope. But a glance at the quantized way these three fields plot on the Ir-Ni diagram (Fig. 5c) as well as the Ni-Au and Co-Au diagrams (Figs. 2a, 2b) makes the last proposal appear implausible.

The modified IIIAB solid (sol) and liquid (liq) tracks plotted on the diagrams in Fig. 5 offer some perspective if not clarity. Looking first at the Ir-Ni diagram (Fig. 5c), we see that the slopes are much too steep to yield useful fits of the MG data. This is the basis of past conclusions that IAB did not form by fractional crystallization. Note the position of the liquid curve. Adding trapped melt to the solid could fill up the compositional space between the solid and liquid curves, but this would still not account for the majority of the MG data.

In contrast, the slope of the solid fractional crystallization (FC) track on the Ir-Au diagram (Fig. 5a) is about the same as the mixing curve; the liquid track is off scale to the right side of the diagram. If we moved these two curves to Au values ~10% lower we could account for the main-group irons by mixing equilibrium solid with minor amounts of melt. Note however that, in such models, the mean composition of the group is the same as the initial melt composition, roughly at 1.3 μg/g Ir and 3 μg/g Au; thus, this FC model would require that the terrestrial sampling of IAB core be strongly biased. Although this cannot be ruled out, the uniform abundance of main-group irons across the entire field suggests the opposite, that a reasonably representative sample set is available. Our interpretation of the Ir-As plot (Fig. 5b) is similar to that for Ir-Au.

Although most of the main-group Ir-X trends are adequately explained by mixing (or unmixing) equilibrium solids and melt, it is clear that the lowest Ir values (0.06 μg/g in Zaffra) cannot be produced by mixing alone if these formed from the same magma as the cluster between the horizontal lines (Fig. 5). The maximum reduction relative to the mean composition that can be achieved in the liquid in a metal-rich system is D_{Ir} (which seems not to have been greater than 4). Since the mean Ir concentration is near 2 μg/g, the lowest Ir content that can be achieved by crystal separation is ≈0.5 μg/g. We therefore

Table 4. A list of IAB properties that must be explained by a successful model.

Property	Implied constraints
Chondritic silicates	Temperatures not hot enough to melt plagioclase or times too short to permit appreciable migration
Silicate plagioclase contents variable from clast to clast	Temperatures (and shear forces) varied on scales of a few tens of cm
Primordial noble gases abundant	High-temperature period too brief to permit diffusive escape of noble gases from trapping sites
Gas-retention ages high	Material cooled to blocking temperatures within 100 ka
$\Delta^{17}O$ values $\leq -0.3‰$	Parental chondritic materials were closely related to carbonaceous chondrites
High FeS contents common	S contents of melts relatively high (perhaps 20 mg/g in MG melt, higher in some others); melt trapping was common
High C contents are common	Appreciable C was available in the source; C played important role in determining solid/liquid distribution ratios for the siderophilic elements
Ir fractionations minor compared to magmatic groups	Fractional crystallization not dominant fractionation mechanism (in S-rich systems, D_{Ir} is high, ≥ 3; a few extreme values may require fractional crystallization)
γ crystals small, 2–40 cm	Cooling through γ-iron stability field too rapid to allow diffusional growth of large crystals
X-Au trends in low-Au subgroups similar to those in MG	Same fractionation scenario applies to each of these four groups

suggest that these low values were formed either (1) in small isolated regions cooling slowly enough to fractionally crystallize the magma and having dimensions large enough that diffusion at lower temperatures was not able to erase the compositional gradients; or (2) from parental melts formed in events that produced much lower Ir contents, as observed in some impact melts documented in ordinary chondrites (Rubin, 1995). Such large fractionations can be produced during impact events by selective volatilization and recondensation at another location of all but the most refractory siderophiles.

6. A SCENARIO: CRYSTAL-SEGREGATION FRACTIONATION IN AN IMPACT-GENERATED MAGMA

6.1. Some Constraints

The main features that need to be explained by a successful IAB model are summarized in Table 4. Among the most important are the elemental fractionations in the metal and the intimate association of noble-gas-rich chondritic silicates with the metal. The chemical fractionations in the four low-Au groups are now well defined. They differ from those in the magmatic groups both in terms of the limited amount of fractionation in each group (with 4 MG exceptions, only a factor of 4 in Ir; only a factor of 1.3 in Au) and the higher number of ungrouped irons occupying the compositional space near the groups.

The fractionations observed in our data sets are almost certainly associated with metallic melts. In the melts that gave birth to the magmatic groups, the cooling was slow enough to permit the magma to remain well mixed (by convective stirring) and thus produce fractional crystallization. For this reason silicates are essentially unknown in the magmatic groups. When present, they are fractionated (not chondritic) and sometimes (like the tridymite veins in IVA Gibeon) appear to be condensates deposited in cracks.

The coarse silicates in IAB irons are commonly chondritic; thus temperatures were generally lower than the plagioclase solidus (brief high-temperature excursions too short to allow melt migration may have occurred). These silicates have high contents of noble gases; for example, the compilation of Schultz and Franke (2000) shows that spallation-corrected primordial ^{36}Ar concentrations $\geq 8 \cdot 10^{-8}$ cm^3 STP g^{-1} have been reported in the silicates of Campo del Cielo, Landes, Pitts, Udei Station, and Zagora. These concentrations are similar to those observed in whole-rock samples of lightly metamorphosed (type-3) ordinary chondrites. Thus the period of time spent at temperatures >1200 K must have been quite brief, otherwise concentrations would be much smaller. Based on their study of MG Bohumilitz, Maruoka et al. (2001) reach a similar conclusion. Although they question whether metallic melts could have ever been present, it seems clear that these are demanded by the observed fractionations, and that there are other possibilities (e.g., survival in silicates that did not reach such high temperatures or in refractory phases such as graphite that were not destroyed during the brief lifetime of the metallic melt).

Ages based on Rb-Sr and Sm-Nd are $\sim 4.5 \pm 0.1$ Ga (Bogard et al., 1968; Takeda et al., 2000). Ages that require gas retention (I-Xe, ^{39}Ar-^{40}Ar) are similar, thus diffusional blocking temperatures for the host phase of K and I were reached on a time scale of ~100 Ma or less (Niemeyer, 1979a, 1979b).

Fine silicates are ubiquitous in irons of the low-Au IAB irons. It appears that, if one searches diligently, one can find 100-μm grains in each iron. And, when larger grain aggregates are found, they generally have chondritic characteristics (the dominant minerals are mafics, the minor plagioclase is albitic). The challenge then is to explain how the metallic melts necessary to produce the observed fractionations could have existed without these silicates separating buoyantly from the metallic melt. In our opinion, this can only mean that the viscosity of the melt became large on a time scale short compared to the time necessary for silicate grains to separate from the melt.

Of course, at constant density of the body, the gravitational field scales linearly with the distance from the center, and buoyant velocities can be quite small near the center of the body. If we assume that the initial melt had a relatively high viscosity of ~50 poise (equivalent to a heavy syrup), the silicate density was 3.1 g cm^{-3}, the metal melt density was 7.7 g cm^{-3}, the bulk density of the body was 3.0 g cm^{-3}, and the distance from the center of the body was 1 km, we calculate that a 100-μm-diameter silicate grain will rise 5.4 m in a year, or 45 cm in a month. Viscosities vary exponentially but moderately with temperature. Pure Fe metal liquid has an activation energy of 44 kJ K^{-1} mol^{-1} (Brandes and Brook, 1992), which requires temperatures to drop ~300 K to change the viscosity

by a factor of 2. In the scenario given below, the initial melt included suspended crystals, and the increase in viscosity with cooling was probably mainly the result of an increase in the fraction of such suspended crystals.

Not only did the melt cool rapidly, the metal also cooled through the γ-iron field at a relatively high rate. Based on differently oriented Widmanstätten patterns, Buchwald (1975) reports IAB γ-iron crystals to have dimensions in the range 2 to 40 cm. These testify to a high-temperature cooling process far more rapid than that experienced by the IIIAB irons, in which the demonstrated sizes of the largest γ-iron crystals are >2 m (Buchwald, 1975).

6.2. Original Mass of the MG Material

An important question is the original mass of MG metal. The problem can be approached by estimating the mass flux of MG material to the Earth and using cosmic-ray ages to estimate the removal (i.e., decay) constant in the equation:

$$-dM/dt = \lambda \cdot \mathrm{M} \quad (1)$$

where d*M*/dt is the rate of mass loss and M is the mass of material in the part of interplanetary space that is feeding MG meteorites to the Earth. There are many assumptions that go into such a calculation; thus, the results are only illustrative. Errors could easily be as much as an order of magnitude.

Iron meteorites account for ~0.04 of the meteorites that fall; this is the value that one obtains from Grady (2000) after elimination of the results for unclassified irons. The fraction of irons that belong to the main group is ~0.15. We therefore calculate that 0.006 of the meteoritic matter accumulating to the Earth consists of MG irons.

As emphasized by various authors and shown as a plot by Kyte and Wasson (1986), evidence from craters suggests that the mass of accreting material per logarithmic mass interval increases with increasing mass. For that reason, the results are quite dependent on upper limit on the mass that one uses. We integrated the mass function recommended by Kyte and Wasson for the mass range 10^2 to 10^{12} g (the upper limit approximately corresponding to the size of the MG Canyon Diablo meteoroid that created Meteor Crater) and obtained a terrestrial MG mass flux of $9.9 \cdot 10^8$ g a^{-1}. We then arbitrarily increased this by a factor of 4 to allow for removal mechanisms other than accretion to the Earth, and by a factor of 2 to approximate the amount that was present immediately after the disruption events that started the cosmic-ray clock running.

The mean MG cosmic-ray age obtained by the ^{40}K–^{41}K method by Voshage (1978) and Voshage and Feldmann (1979) is 712 Ma. However, Lavielle et al. (1999) showed that these ages are systematically high by factors of 1.4 to 1.5. We therefore used 500 Ma as the mean MG cosmic-ray age, leading to a decay constant of $2 \cdot 10^9$ a^{-1}. From this removal constant and the estimated removal flux 500 Ma ago, we calculate a mass of MG material of $2.4 \cdot 10^{16}$ g, or (at a density of ≈ 8 g cm^{-3}) a volume of 3 km^3. If, as Wasson and Ouyang (1990) suggested for Canyon Diablo, the largest members of the set include large quantities of silicates, then the mean density might be around 4 g cm^{-3} and the volume 6 km^3. Of course, as already stated, these estimates are very rough.

6.3. Heat Source

The distribution in compositional space of irons from the IAB complex is much more diffuse than the distributions observed in the magmatic groups and nearby compositional space. This and the preservation of chondritic compositions, the preservation of planetary-type rare gases in the silicates, the retention of silicate grains in the melt, and the small sizes of γ-iron crystals are best understood in terms of rapid heating and cooling. This temperature history seems best provided by large impact events.

It is clear, however, that these events were very different from the cratering events that have been well documented on Earth, Moon and, to lesser degrees, on other planets and satellites. Such impacts of low-porosity projectiles into low-porosity targets are relatively inefficient at generating melt (Keil et al., 1997). Most of the impact energy goes into translational motion of crater ejecta, and the most heated material is ejected at velocities that exceed the escape velocity from the asteroid.

In contrast, if the target asteroid is highly porous, the projectile may penetrate relatively deep, and much of the energy may be retained within the body, both because compression of porous materials leads to a more efficient conversion of kinetic energy to heat (Melosh, 1988, p. 41) and because the heated material is largely buried under insulating (mega) regolith that does not escape the body. As noted by Wasson (1991), the ideal target for producing melt is highly porous (this maximizes the conversion of kinetic impact energy to heat), fine grained (the centers of grains must be heated by conduction), and dry (wet targets lose much of the deposited heat in the form of escaping steam). Because it seems clear that most materials agglomerated in the solar nebula were highly porous (as well as fine-grained and dry), such ideal targets must have been common early in solar-system history. Even after the collisional compaction of these early materials, the densities of some asteroids such as Mathilde indicate high (micro or macro) porosities today (1.3 g cm^{-3}; Veverka et al., 1999).

The mean impact velocity in the asteroid belt is ~5 km s^{-1} (Bottke et al., 1994), and the primordial value was probably about the same 4.6 Ga ago. There is a considerable spread in impact velocities, from ~1 to 10 km s^{-1}. The kinetic energy deposited by a 1-g projectile moving at 5 km s^{-1} is 12.5 kJ; it requires ~1.3 kJ g^{-1} to melt chondritic matter (Wasson, 1985, p. 77); thus if this energy is entirely converted to heat, there is enough to melt ~9 g of target plus projectile. For a typical asteroid in the inner part of the Asteroid Belt ~20% of impact velocities are >7 km s^{-1} (W. Bottke, personal communication, 2001); these impacts could melt an amount 2× larger.

Complete focusing of heat into the immediate surroundings is, of course, unrealistic. Even if no ejecta escapes the body, some heat will be deposited into more distant materials. Because heat transport by conduction is a slow process, the efficiency of melt production should increase with the size of the event. Although we are unable to make a precise estimate, we suggest that large (>100-m) projectiles are capable of producing appreciable melting, the amounts being comparable to the mass of the projectile.

6.4. Melt and Crystal Transport

As shown particularly well in large sections of the Portales Valley chondrite (e.g., Fig. 2 of Rubin et al., 2001), metallic

Table 5. Assumed D values and initial melt concentrations for the main group. These values were used to generate the solid/melt mixing curves plotted in Figs. 5 and 6. Concentrations in μg/g except Co and Ni in mg/g.

Element	Co	Ni	Ga	Ge	As	W	Ir	Au
Assumed D value	0.90	0.80	1.7	2.7	0.42	2.9	3.0	0.74
Main-group mean	4.64	68.9	86.5	359	12.8	1.22	2.60[a]	1.55
100% melt	4.81	74.1	68.9	221	16.1	0.72	1.53	1.71
30% melt, 70% solid	4.47	63.8	102.6	483	9.58	1.68	3.67	1.40

[a] One high and six low Ir values excluded from mean; see text.

impact melts are common in impact-altered chondrites. According to Stöffler et al. (1991), these can form at lower shock pressures than silicate melts. Our impression is that metallic melts are also more common than silicate melts in chondrites that show massive veining (veins as much as several mm wide and several cm long). It thus seems plausible that metal-troilite is more easily melted than silicates during impact events.

Because silicate and metal melts are immiscible and grossly different in density, metallic melts will tend to segregate. If their viscosities are low, they will tend to flow downward through the chondritic rubble until the leading edge has cooled (probably by heat exchange with cooler silicates) sufficiently that it no longer flows, at which time some ponding occurs. Note that this process suggests that the melt may stop flowing near rubble that experienced less heating, a scenario that helps explain why silicate clasts seem less thermally altered (and retained noble gases) than were the chondritic precursors heated to generate the melts.

It is probable that there were some metal grains that did not fully melt, and thus that there were abundant crystallization nuclei in the melt. These would have gradually grown in size as the melt cooled. The presence of these grains in a subliquidus melt will cause viscosities to rise very quick upon cooling. We suggest that the melt only needed to cool $\sim$50 K to trap the 100-μm silicates. In a deeply buried melt inside a body in which radial temperature gradients were established by conduction towards the external surface such rapid cooling would not be possible, but a plausible scenario for rapid cooling of an impact-generated metallic melt migrating through (and exchanging heat with) crushed silicates that were initially $>$100 K cooler could surely be constructed.

Returning to the migrating melt scenario, coagulation of these metallic grains may have produced sizes that were too large to pass through narrow passages in the rubble. These coagulated materials would have trapped some of the melt. This is our scenario for producing fractionation by crystal separation. If the metallic grains were still small at the time the coagulated materials were segregated, the solids and melt would have been more or less in equilibrium throughout the settling process.

We should note that the crystal segregation process envisioned here is fundamentally different from the fractional crystallization that occurred in the magmatic groups. Fractional crystallization requires that the volume of the melt be semi-infinite compared to the volume of the growing solid interface, and that the melt remained well-mixed during differential crystallization and sequestering of the evolving solid. In contrast, our crystal-segregation process requires that the relative volumes of melt and solids be similar and that the compositions of the solid and liquid undergo only minor evolution during crystallization. This process is also very different from the melt-trapping events inferred to have played an important role in the formation of group IIIAB (Wasson, 1999). The latter involved only a tiny fraction of a large magma, whereas in crystal segregation the size of the melt is much smaller and the entire melt is involved.

6.5. Crystal-segregation Fractionation

Because the process we envision is very different from previously published fractionation scenarios (Wasson et al., 1980; McCoy et al., 1993), it seems useful to describe it starting with the point where the metallic melt (and its load of tiny crystals) has formed but no bulk fractionation has yet occurred. If we assume that the main group is well sampled, the initial bulk composition of this melt is the mean of the main-group data tabulated in Table 2. This value is listed in Table 5. We assume that fine ($\leq$100 μm) silicates were distributed uniformly throughout the melt.

We also assume that, initially and at all subsequent times, the coexisting solid and liquid were in equilibrium. Because of the moderately large amount of scatter, particularly on the Ir-X diagrams in Figure 5, we are sure that this assumption can only be considered a rough approximation.

To put perspective on the elemental fractionations, we point out some simple consequences of the model. If we assume that the initial melt was essentially pure melt, i.e., consisted of $\sim$99% liquid and $\sim$1% solids, then the initial liquid would still have the MG bulk composition. If any of this tiny solid fraction were to separate, it would have elemental concentrations equal to $D_X \cdot X_m$, where D_X is the solid/liquid weight ratio and X_m is the MG mean concentration of element X. If, in contrast, the melt had crystallized and consisted of 1% liquid and 99% solids, then the solids would have the MG bulk composition, and any liquid that managed to escape would have elemental concentrations equal to X_m/D_X.

It is improbable that these illustrative fractionations were ever realized, i.e., it is unlikely that such early pure solids or late pure liquids could separate from the relatively rapidly cooling system that we envision. Small quantities of metal might be left behind as the liquid drained downwards, but these would mainly consist of silicates associated with minute amounts of adhering and interstitial melt, and the solid metal would probably have such small dimensions that such materials would not be designated iron meteorites when they fall. Small amounts of late liquids would only separate if there were hydraulic pressure forcing them out of a solid matrix, but liquids in rubble-pile asteroids will feel no overburden pressure.

We have therefore based our calculations on the following oversimplified model. We assume that all the crystal-segregation fractionation occurred at the same time after some fraction F of the melt had crystallized. Until this point crystallization had occurred much faster than the buoyant separation of solids (note that if we had metal and silicate grains the same size, the buoyant [downward] velocity of the metal would be ~30× slower than the upward velocity of the silicates) and the composition of m-size or larger parcels of the solid-melt mix would still preserve the initial composition (i.e., the mean MG composition). Separation of crystals and melt now occurred, producing the main-group elemental fractionations.

In addition to assuming that the MG mean represents the bulk initial composition of the melt plus its incipiently crystallizing solids, we assume that the high-Au extreme of the main group approximates the composition of this melt. Concentrations of key elements in this initial melt are listed in Table 5.

We can now write the mass-balance equation

$$X_m = F \cdot X_s + (1 - F) \cdot X_I \quad (2)$$

where X_s and X_l refer to the concentrations of X in the solid and liquid, respectively. Because $X_s = D_X X_l$ we can also write this equation:

$$X_m = F \cdot D_X \cdot X_I + (1 - F)X_I \quad (3)$$

Collecting terms yields

$$X_m = X_l \cdot (1 - F + F \cdot D_X) = X_l \cdot [1 + F \cdot (D_X - 1)] \quad (4)$$

The above assumptions provide us with X_m and X_l for each element. There is no unique solution. Instead, we now roughly estimated D_X values by using the available laboratory data and estimates based on fitting trends in iron meteorite groups, then adjusted these to give ranges in F that seemed reasonable based on viscosity and Stokes' law settling arguments.

Figure 6 shows simplified versions of six of the diagrams shown in Figures 2 and 3. Only the four low-Au groups are plotted; grouplets and ungrouped irons (17 solos and 10 in duos) were deleted. Because, as discussed above, the main group is much better defined than the subgroups, we limit our detailed discussion to reproducing its trends. The curves through the MG data sets show fits obtained by the above crystal-segregation model.

The parameters used in these fits are listed in Table 5. After trying a range of D_{Au} values we set this parameter at 0.74, then fit the other parameters. From these D_X values, the MG mean composition, and estimates of the liquid composition we calculated the degree of crystallization at the outset of the crystal-segregation process to be 35%. These fit parameters are not unique; the trends can be modeled with differing degrees of crystal separation and different D_X values. We chose D_X values based on laboratory studies (Jones and Malvin, 1990) and based on ranges we inferred from our studies of the magmatic groups IIIAB (Wasson, 1999) and IVA (Wasson and Richardson, 2001). Because the main-group melt clearly had a high C content (C/Fe atomic ratio >0.01) and because very little is known about how C concentration affects D_X values, it does not appear to be possible to use published experimental results to narrowly constrain ranges within which D_X values should be found.

There is a tradeoff between higher (and perhaps more plausible) D_X values and lower (and possibly more plausible) ranges in degrees of solid segregation. As noted above, we assumed that the high-Au (1.7 mg/g) extreme of the MG is pure liquid. We then calculated that the low-Au (1.4 mg/g) extreme corresponds to a mix of 30% melt and 70% solids. These estimates are consistent with our impression that the range in melt (and S) contents within the main group might be around a factor of 4 with bulk S correlating with Au content. We note, however, that the S content of most irons is probably lower. If we had chosen higher D_X values, the amount of liquid at the low-Au extreme would have been lower and the range of S contents would have been larger. We argue that any other team that would try to incorporate S estimates, plausibility arguments about viscosity and coagulation to fit this many elements by such a model would choose values not very different than those listed in Table 4.

6.6. Fractional Crystallization

As discussed above and illustrated in Figure 5, a few IAB irons with compositions consistent with membership in the main group have Ir contents that are well below the main-group range. We picture that these could have formed in rare cases where pockets of melt cooled slowly enough to allow fractional crystallization. If the silicates were the chief heat sink, this could indicate that these melts were surrounded by silicates that were hotter than those near the bulk of the group. Although these regions were small compared to the total main-group volume, the size of the fractionated regions must have been >1 m, large enough to prevent compositional leveling by solid-state diffusion, which may have produced appreciable transport over distances of 50 to 100 cm.

There are some cases of resolvable compositional variations within individual meteorites. The largest confirmed range in the IAB complex is about a factor of 1.2 in Ir among the Canyon Diablo irons (Wasson and Ouyang, 1990); because of the very large size (ca. 50 m) of this meteoroid, these different compositional regions may have been widely separated.

6.7. Compositional Differences between the Subgroups and the Main Group

There are quite large differences in the elemental concentrations between the low-Ni subgroups and the main group. Here we will limit the discussion to eight elements, the seven plotted in Fig. 6 and Ir. We will limit the comparison with the main group to sLH and sLM, the two subgroups most widely separated from the MG in composition.

There is relatively little fractionation in Au among these three groups (the mean Au content in sLH is 1.18× MG, that in sLM is 1.09× MG), and because most of the compositional fields show roughly parallel trends, it seems reasonable to compare the elemental concentrations at the same Au concentration of 1.7 μg/g. Our estimates of these ratios are listed in Table 6. The most extreme differences in these sLH/MG ratios range from 2.3 in Ni to 0.017 in Ge.

Because of the similarities in numerous properties including structure (e.g., silicate abundance), $\Delta^{17}O$, and metal compositional trends, it is appropriate to examine the possibility that variations in formation processes could have produced these groups from the same carbonaceous chondrite starting materials.

Wasson et al. (1980) and Choi et al. (1995) suggested that variations in the degree of impact melting could lead to the

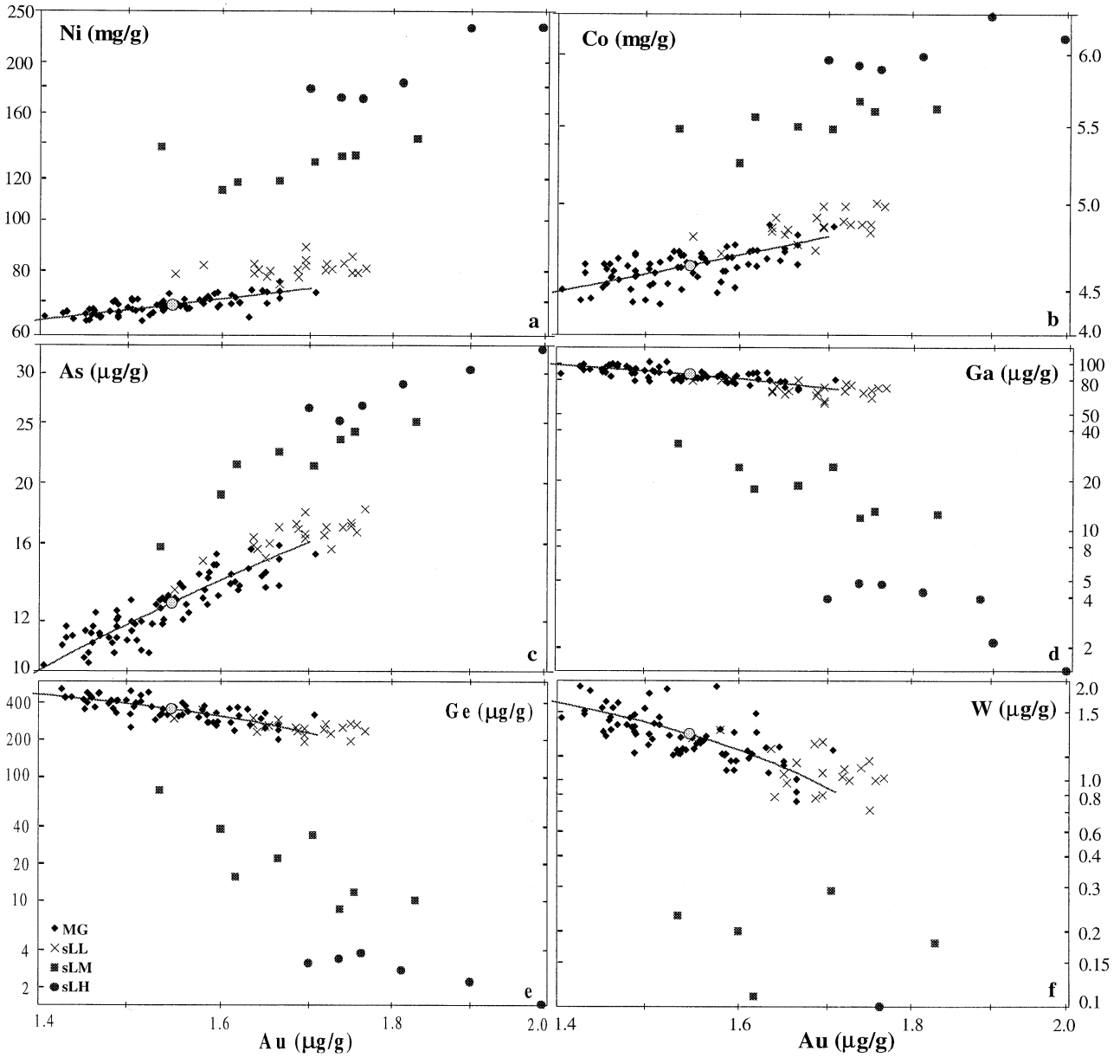

Fig. 6. These six element-Au diagrams are the most useful for discussing compositional differences among the main group and the low-Au subgroups, and the possible fractionation processes that were involved in their formation. The curves drawn through the main group show the loci of points produced by mixing a liquid with a composition near the high-Au extreme of the group (right end of the mixing curve; elemental contents listed in Table 4) with an equilibrium solid whose Au content is below the lower Au limit of the diagram. The low-Au extreme of the main group corresponds to a mix containing ≈80% of this solid.

main observed compositional differences in IAB (as then constituted). For example, Ni contents in low-temperature melts might be high because nebular condensation of S on metal would require removal of Fe from grain surfaces leading to an enhanced Ni content in the layer immediately below the FeS. Surficial layers of nebular metal might have low contents of refractory Ir because the Ir-rich condensates were sequestered in silicates or because the cores of incompletely melted Fe-Ni grains were Ir-rich (if refractory metal grains served as condensation nuclei).

It was suggested that Ga and Ge may have mainly condensed from the nebula as oxides, and that these may have only been reduced in larger, high-temperature melting events. Tungsten is refractory under reducing conditions and volatile under oxidizing conditions; its variations could result because W was with Ir in refractory condensates, or because W condensed as an oxide and fractionated together with Ga and Ge. In general, impact-generated gases should be much more oxidizing than the H_2-dominated solar nebula. As a result, elements such as Ga, Ge, and W that form volatile oxides may be transported as gases during impact events, thus producing either enrichments or depletions relative to the parental materials (Rubin, 1999).

Based on these arguments, we conclude that it is plausible

Table 6. Comparison of elemental concentrations in subgroups sLH and sLM with those in the main group. Ratios estimated at a Au concentration of 1.7 μg/g for each group.

Element	Co	Ni	Ga	Ge	As	W	Ir
sLH/MG ratio	1.23	2.3	0.07	0.017	1.6	0.14	0.05
sLM/MG ratio	1.15	1.7	0.24	0.077	1.3	0.28	0.22

that the low-Au subgroups and grouplets originated on the same parent asteroid as the main group. Because this easily accounts for the similar $\Delta^{17}O$ values, it is our preferred working model.

6.8. Comparisons with Previous IAB Models

Numerous research teams have attempted to account for the textural and compositional properties of the irons in the IAB complex. A major difference between our current model and those by other teams (Benedix et al., 2000; Takeda et al., 2000; McCoy et al., 1993; Kracher, 1985) is that we infer that the metallic melt was mainly produced by impact heating, whereas the other teams prefer internal heat sources such as the decay of ^{26}Al.

Benedix et al. (2000) use ^{26}Al to produce five lithologies, then use impacts to mix these while the metallic portions are still partly or largely molten. They mention that the fractionation of the metal was produced by fractional crystallization but give no details. Our model differs mainly in using impacts to produce the melting and to generate silicate clasts (although we could not rule out multiple generations of impacts). Furthermore, we use crystal segregation to rapidly fractionate the metal in a way that allows the melt viscosity to increase fast enough to retain its suspended fine silicates.

Wasson et al. (1980) suggested that each IAB or IIICD iron formed as a separate melt pool having sizes ranging from centimeters to tens of meters. Our improved data set (which shows compact fields and well-defined positive or negative trends in the IAB main group, as well as parallel trends in three subgroups having similar Au contents and, more important, similar $\Delta^{17}O$ values) requires a major modification of this model; it now appears probable that the entire main group formed as a single melt body. The compositional differences among the various low-Au groups seem best interpreted as the result of formation as different melt pools, possibly within a single parent asteroid.

7. IMPACT MELTING AS A GENERAL PROCESS RESPONSIBLE FOR GENERATING DIFFERENTIATED METEORITES ON CARBONACEOUS CHONDRITE ASTEROIDS

There are a large number of differentiated meteorite classes that have O-isotopic compositions linking them to the carbonaceous chondrites ($\Delta^{17}O \leq -0.4‰$). In addition to the silicate-bearing irons in the IAB complex and their near relatives the winonaites, these include the ureilites, the lodranites, the acapulcoites, the bencubbinites, the Eagle-Station pallasites, and numerous ungrouped silicate-rich differentiated meteorites (e.g., Hammadah al Hamra 237). A feature that many of these silicate-rich meteorites have in common is that they are compositionally closely related to chondrites; in many cases the difference in bulk silicate compositions can largely be accounted for by the loss or gain of a plagioclase-rich melt.

It is extremely difficult to produce such materials from chondritic parents by a heat source such as ^{26}Al that releases its heat slowly over a period of 1 Ma or longer; deeply buried chondritic materials would reach the same temperature at the same time. Because mechanical fractionations such as the migration of basaltic melts into voids or upwards through cracks or the gravitational separation of immiscible metal and silicate liquids occur on time scales that are many orders of magnitude shorter than those of the radioactive heat sources, these effects should occur more or less uniformly throughout large (km-size) regions.

If such an internally heated system produces minimal melting, the first physical phase separations consist of the loss of a plagioclase-rich silicate liquid and/or an FeS-rich metallic liquid, leaving behind an intimate mixture of mafic silicates and metal; textures would be coarser than those in the precursor chondritic silicates. This process could explain some features of these differentiated meteorites, but it cannot explain the situation observed in Campo del Cielo in which the degree of loss of a low-temperature plagioclase-rich melt is highly variable on a scale of centimeters (Wlotzka and Jarosewich, 1977).

If extensive (perhaps 50%) melting is produced, the asteroidal body will differentiate into a central core, mantle, and crust (Taylor et al., 1993). It appears that, in the iron-meteorite parent asteroids, such cores commonly fractionally crystallized. Thus a second problem with an internal (e.g., ^{26}Al) heat source is that the heat release must be carefully controlled. Too little heat yields no phase separation, too much produces silicate-free magmas, extensively fractionated iron-meteorite suites such as the IIIAB irons, and classic igneous rocks such as the basaltic eucrites.

In summary, even with small degrees of heating/melting produced by ^{26}Al decay it seems impossible to preserve chondritic compositions in adjacent samples. In such slowly heated (and even more slowly cooled) material, it also seems impossible to avoid the escape of rare gases (i.e., from the sites that contain primordial gas or ^{40}Ar produced by in site decay of ^{40}K). Primordial gas has been largely lost from eucrites and diogenites; where much gas has been retained (as in ureilites), it implies a much more rapid temperature history. Many additional problems occur if extensive melting occurs; these include the fractional crystallization of the metal and the buoyant separation of small silicates from the metallic melt, or small metal grains from silicate melts.

For the above reasons and also because of textural evidence there have been many proposals suggesting an impact origin of features preserved in the differentiated meteorites (such as lodranites and ureilites) that were formed by the incomplete melting of carbonaceous chondrites. We suggest that there are no proven exceptions to this generalization.

8. SUMMARY

A reevaluation of data on 12 elements in IAB, and closely related iron meteorites (including those earlier called IIICD) reveals the presence of a well-defined main group, three low-Au and two high-Au subgroups, two low-Au grouplets, and 25 related ungrouped irons. The compositional trends are most sharply defined on Ni-Au diagrams, but differences can also be recognized on several diagrams (Co-Au, As-Au, Ga-Au, Ge-Au, W-Au, and Sb-Au). Because it includes 70+ members, the trends in the main group are particularly well defined. Although there is more uncertainty in the subgroup

trends, it appears that their element-Au fields are roughly parallel to those in the main group. This implies that the trends in each group were produced by the same basic processes.

There are numerous features in IAB irons that demand a rapid traversal of the high temperatures necessary to generate the metallic melt. Among these are the retention in the silicates of chondritic compositions and large amounts of planetary and radiogenic gases. The small sizes of the γ-iron crystals parental to the octahedral structures imply rapid cooling during the traversal of this T-X field.

A major problem facing those creating IAB models is how to account for the retention of small ($\leq$100 μm) silicate grains in the metallic melts of the IAB complex since these should separate buoyantly on time scales of a year or less. In our view, it is not possible to avoid silicate separation if the heat source is internal (e.g., ^{26}Al). Our model retains these silicates within a hot impact-generated melt both by stirring the melt as it moves downward through the largely chondrite rubble, and by allowing viscosity to rise rapidly as the melt leaks heat to the cooler rubble and crystallization occurs.

Acknowledgments—We thank Finn Ulff-Møller, Byeon-Gak Choi, Eric Jerde, Xinwei Ouyang, John Richardson, and Jianmin Wang for assistance in gathering the INAA data and Alan Rubin and Bob Clayton for petrographic and O-isotope data and discussions. Detailed and helpful reviews were provided by Nancy Chabot and Alfred Kracher. A number of curators provided samples, often on relatively short notice. Technical support was provided by Sydney Zhang, Linda Lee, and Kimberly Jo. This research was mainly supported by NASA grant NAG5-4331 and NASA grant NAG5-10421.

Associate editor: C. Koeberl

REFERENCES

Benedix G. K., McCoy T. J., Keil K., and Love S. G. (2000) A petrologic study of the IAB iron meteorites: Constraints on the formation of the IAB-Winonaite parent body. *Meteorit. Planet. Sci.* **35,** 1127.

Boesenberg J. S., Davis A. M., Prinz M., Weisberg M. K., Clayton R. N., and Mayeda T. K. (2000) The pyroxene pallasites, Vermillion and Yamato 8451: Not quite a couple. *Meteorit. Planet. Sci.* **35,** 757–769.

Bogard D., Burnett P., Eberhardt P., and Wasserburg G. J. (1968) ^{40}Ar-^{40}K Ages of silicate inclusions in iron meteorites. *Earth Planet. Sci. Lett.* **3,** 275–283.

Bottke W. F., Nolan M. C., and Greenberg R. (1994) Velocity distributions among colliding asteroids. *Icarus* **107,** 255–268.

Brandes E. A. and Brook G. B. (1992) *Smithells Metal Reference Handbook*. 7th ed. Butterworth-Heinemann.

Buchwald V. F. (1975) *Handbook of Iron Meteorites*. Univ. California Press 1418 pp.

Choi B., Ouyang X., and Wasson J. T. (1995) Classification and origin of IAB and IIICD iron meteorites. *Geochim. Cosmochim. Acta* **59,** 593–612.

Clayton R. N. and Mayeda T. K. (1996) Oxygen isotope studies of achondrites. *Geochim. Cosmochim. Acta* **60,** 1999–2017.

El Goresy A. (1965) Mineralbestand und Strukturen der Graphit-und Sulfideinschlüsse in Eisenmeteoriten. *Geochim. Cosmochim. Acta* **29,** 1131–1151.

Fuchs L. H., Olsen E., and Henderson E. P. (1967) On the occurrence of brianite and panethite, two new phosphate minerals from the Dayton meteorite. *Geochim. Cosmochim. Acta* **31,** 1711–1719.

Goldberg E., Uchiyama A., and Brown H. (1951) The distribution of nickel, cobalt, gallium, palladium and gold in iron meteorites. *Geochim. Cosmochim. Acta* **2,** 1–25.

Grady M. M. (2000) *Catalogue of Meteorites*. 5th ed. Cambridge Univ. Press 689 pp.

Haack H. and Scott E. R. D. (1993) Chemical fractionations in group IIIAB iron meteorites: Origin by dendritic crystallization of an asteroidal core. *Geochim. Cosmochim. Acta* **57,** 3457–3472.

Jones J. H. and Malvin D. J. (1990) A nonmetal interaction model for the segregation of trace metals during solidification of Fe-Ni-S, Fe-Ni-P and Fe-Ni-S-P alloys. *Metal. Trans.* **21b,** 697–706.

Kallemeyn G. W. and Wasson J. W. (1985) The compositional classification of chondrites: IV. Ungrouped chondritic meteorites and clasts. *Geochim. Cosmochim. Acta* **49,** 261–270.

Keil K., Stöffler D., Love S. G., and Scott E. R. D. (1997) Constraints on the role of impact heating and melting in asteroids. *Met. Planet. Sci.* **32,** 349–363.

Kelly K. R. and Larimer J. W. (1977) Chemical fractionations in meteorites-VIII: Iron meteorites and the cosmochemical history of the metal phase. *Geochim. Cosmochim. Acta* **41,** 93–111.

Kracher A. (1982) Crystallization of a S-saturated Fe, Ni-melt, and the origin of iron meteorite groups IAB and IIICD. *Geophys. Res. Lett.* **9,** 412–415.

Kracher A. (1985) The evolution of partially differentiated planetesimals: Evidence from iron meteorite groups IAB and IIICD. *Proc. Lunar Planet. Sci. Conf.* **15,** C689–C698.

Kracher A. and Kurat G. (1977) Silicates in the Carlton (IIIC) iron meteorite and possible relations to group IAB. *Meteoritics* **12,** 282–283 (abstract).

Kracher A., Malissa H., Weinke H. H., and Kiesl W. (1975) Über die Zusammensetzung meteoritischen Kupfers. *Mikrochim. Acta* (Suppl. 6) 251–256.

Kracher A., Willis J., and Wasson J. T. (1980) Chemical classification of iron meteorites—IX. A new group (IIF), revision of IAB and IIICD, and data on 57 additional irons. *Geochim. Cosmochim. Acta* **44,** 773–787.

Kyte F. T. and Wasson J. T. (1986) Accretion rate of extraterrestrial matter: Iridium deposited 33 to 67 million years ago. *Science* **232,** 1225–1229.

Lavielle B., Marti K., Jeannot J.-P., Nishiizumi K., and Caffee M. (1999) The ^{36}Cl-^{36}Ar-^{40}K-^{41}K records and cosmic ray production rates in iron meteorites. *Earth Planet. Sci. Lett.* **170,** 93–104.

Lewis C. F. and Moore C. B. (1971) Chemical analyses of thirty-eight iron meteorites. *Meteoritics* **6,** 195–205.

Lindner L. and Buchwald V. F. (1985) Algarrabo, a new iron meteorite from Chile. *Meteoritics* **20,** 699 (abstract).

Lovering J. F., Nichiporuk W., Chodos A., and Brown H. (1957) The distribution of gallium, germanium, cobalt, chromium, and copper in iron and stony-iron meteorites in relation to nickel content and structure. *Geochim. Cosmochim. Acta* **11,** 263–278.

Malvin D. J., Wang D., and Wasson J. T. (1984) Chemical classification of iron meteorities—X. Multielement studies of 43 irons, resolution of group IIIE from IIIAB, and evaluation of Cu as a taxonomic parameter. *Geochim. Cosmochim. Acta* **48,** 785–804.

Maruoka T., Matsuda J.-I., and Kurat G. (2001) Abundance and isotopic composition of noble gases in metal and graphite of the Bohumilitz IAB iron meteorite. *Meteorit. Planet. Sci.* **36,** 597–609.

McBride K., Clarke R. S., and McCoy T. (2000) EET96009: Description. *Antarct. Meteorit. Newsl.* **23,** 15.R. S.

McCoy T. J., Keil K., Scott E. R. D., and Haack H. (1993) Genesis of the IIICD iron meteorites: Evidence from silicate-bearing inclusions. *Meteoritics* **28,** 552–560.

Melosh H. J. (1988) *Impact Cratering: A Geologic Process*. Oxford Univ. Press, p. 41.

Moore C. B., Lewis C. F., and Nava D. (1969) Superior analyses of iron meteorites. In *Meteorite Research* (ed. P. M. Millman), pp. 738–748. Reidel.

Niemeyer S. (1979a) ^{40}Ar-^{39}Ar dating of inclusions from IAB iron meteorites. *Geochim. Cosmochim. Acta* **43,** 1829–1840.

Niemeyer S. (1979b) I-Xe dating of silicate and troilite from IAB iron meteorites. *Geochim. Cosmochim. Acta* **43,** 843–860.

Prinz M., Nehru C. E., and Delaney J. S. (1982) Silicate inclusions in irons and metal-silicate assemblages. *Lunar Planet. Sci.* **13,** 632–633 (abstract).

Prinz M., Nehru C. E., Delaney J. S., Weisberg M., and Olsen E. (1983) Globular silicate inclusions in IIE irons and Sombrerete: Highly fractionated minimum melts. *Lunar Planet. Sci.* **14,** 618–619 (abstract).

Rubin A., Kallemeyn G. W., and Wasson J. T. (2002) A IAB-complex iron meteorite containing low-Ca clinopyroxene: Northwest Africa 468 and its relationship to lodranites and formation by impact melting. *Geochim. Cosmochim. Acta* (in press).
Rubin A. E. (1994) Metallic copper in ordinary chondrites. *Meteoritics* **29,** 93–98.
Rubin A. E. (1995) Petrologic evidence for collisional heating of chondritic asteroids. *Icarus* **113,** 156–167.
Rubin A. E. (1999) Formation of large metal nodules in ordinary chondrites. *J. Geophys. Res.* **104,** 30799–30804.
Rubin A. E., Ulff-Møller F., Wasson J. T., and Carlson W. D. (2001) The Portales Valley meteorite breccia: Evidence for impact-induced melting and metamorphism of an ordinary chondrite. *Geochim. Cosmochim. Acta* **65,** 323–342.
Schultz L., and Franke L. (2000) Helium and argon in meteorites: A data collection unpublished compilation: at www.mpck-mainz.mpg.de/~kosmo/schultz/schultz.htm.
Scott E. R. D. (1972) Chemical fractionation in iron meteorites and its interpretation. *Geochim. Cosmochim. Acta* **36,** 1205–1236.
Scott E. R. D. and Bild R. W. (1974) Structure and formation of the San Cristobal meteorite, other IB irons and group IIICD. *Geochim. Cosmochim. Acta* **38,** 1379–1391.
Scott E. D. and Wasson J. T. (1975) Classification and properties of iron meteorites. *Rev. Geophys. Space Phys.* **13,** 527–546.
Scott E. R. D. and Wasson J. T. (1976) Chemical classification of iron meteorites—VIII. Groups IC, IIE, IIIF and 97 other irons. *Geochim. Cosmochim. Acta* **40,** 103–115.
Stöffler D., Keil K., and Scott E. R. D. (1991) Shock metamorphism of ordinary chondrites. *Geochim. Cosmochim. Acta* **55,** 3845–3867.
Takeda H., Bogard D. D., Mittlefehldt D. W., and Garrison D. H. (2000) Mineralogy, petrology, chemistry, and ^{39}Ar-^{40}Ar and exposure ages of the Caddo County IAB iron: Evidence for early partial melt segregation of a gabbro area rich in plagioclase-diopside. *Geochim. Cosmochim. Acta* **64,** 1311–1327.
Taylor G. J., Keil K., McCoy T., Haack H., and Scott E. R. D. (1993) Asteroid differentiation: Pyroclastic volcanism to magma oceans. *Meteoritics* **28,** 34–52.
Veverka J., Thomas P., Harch A., Clark B., Bell J. F., Carcich B., and Joseph J. (1999) NEAR encounter with asteroid 253 Mathilde: Overview. *Icarus* **140,** 3–16.
Voshage H. (1978) Investigations on cosmic-ray-produced nuclides in iron meteorites, 2. New results on ^{41}K/^{40}K-^{44}He/^{21}Ne exposure ages and the interpretation of age distributions. *Earth Planet. Sci. Lett.* **40,** 83–90.
Voshage H. and Feldmann H. (1979) Investigations on cosmic-ray-produced nuclides in iron meteorites, 3. Exposure ages, meteoroid sizes and sample depths determined by mass spectrometric analyses of potassium and rare gases. *Earth Planet. Sci. Lett.* **45,** 293–308.
Wasson J. T. (1970) The chemical classification of iron meteorites—IV. Irons with Ge concentrations greater than 190 ppm and other meteorites associated with group I. *Icarus* **12,** 407–423.
Wasson J. T. (1972) Parent-body models for the formation of iron meteorites. *Proc. Int. Geol. Cong.* **24,** (15) 161–168.
Wasson J. T. (1974) *Meteorites—Classification and Properties*. Springer 316 pp.
Wasson J. T. (1985) *Meteorites: Their Record of Early Solar System History*. Freeman p. 77.
Wasson J. T. (1991) Layered tektites: A multiple impact origin for the Australasian tektites. *Earth Planet. Sci. Lett.* **102,** 95–109.
Wasson J. T. (1999) Trapped melt in IIIAB irons: Solid/liquid elemental partitioning during the fractionation of the IIIAB magma. *Geochim. Cosmochim. Acta* **63,** 2875–2889.
Wasson J. T., Choi B.-G., Ulff-Møller F., and Jerde E. (1998) Chemical classification of iron meteorites: XII. New members of the magmatic groups. *Geochim. Cosmochim. Acta* **62,** 715–724.
Wasson J. T. and Ouyang X. (1990) Compositional range in the Canyon Diablo meteoroid. *Geochim. Cosmochim. Acta* **54,** 3175–3183.
Wasson J. T., Ouyang X., Wang J., and Jerde E. (1989) Chemical classification of iron meteorites: XI. Multi-element studies of 38 new irons and the high abundance of ungrouped irons from Antarctica. *Geochim. Cosmochim. Acta* **53,** 735–744.
Wasson J. T. and Richardson J. W. (2001) Fractionation trends among IVA iron meteorites: Contrasts with IIIAB trends. *Geochim. Cosmochim. Acta* **65,** 951–970.
Wasson J. T. and Schaudy R. (1971) The chemical classification of iron meteorites–V. Groups IIIC and IIID and other irons with germanium concentrations between 1 and 25 ppm. *Icarus* **14,** 59–70.
Wasson J. T., Willis J., Wai C. M., and Kracher A. (1980) Origin of iron meteorite groups IAB and IIICD. *Zeits. Naturforsch.* **35a,** 781–795.
Wlotzka F. and Jarosewich E. (1977) Mineralogical and chemical compositions of silicate inclusions in the El Taco, Campo del Cielo, iron meteorite. *Smithsonian Contr. Earth. Sci.* **19,** 104–125.
Young E., Coutts D. W., and Kapitan D. (1998) UV laser ablation and irm-GCMS microanalysis of ^{18}O/^{16}O and ^{17}O/^{16}O with application to a calcium-aluminium-rich inclusion from the Allende meteorite. *Geochim. Cosmochim. Acta* **62,** 3161–3168.

APPENDIX A: UNGROUPED IRONS CLOSELY RELATED TO IAB

The compositional fields around the main group and the five subgroups are rich in ungrouped irons. As discussed in section 3, our criteria for separating these from the three groups were mainly based on the taxonomic elements plotted against Au in Figure 2. In some cases we also needed to use one or more of the four elements plotted in Figure 3 to confirm the ungrouped nature. As noted above, in contrast to the practice of Wasson et al. (1980) and Choi et al. (1995), our current view is that Ir (plotted in Fig. 5) is of secondary importance for classification; because of suspected sampling problems Cu (Fig. 3c) is also of limited value.

In Figure A1 we show the positions of the 27 ungrouped irons plotted on the same four fields used in Figure 2. To bring out the positions of the ungrouped irons, we eliminated individual points for the group members and instead outlined the fields they occupy. The positions of the irons in the two grouplets are shown by small symbols.

A1. Five Duos

Plotted as filled triangles on Figures 2, 3, and A1 are five pairs of irons; the members of these duos are closely related to each other, but not closely related to the groups or the solo irons discussed below. For convenience in locating these irons on the figures, they are discussed in order of increasing Au contents, which are listed (in units of μg/g) immediately after the names.

The lowest Au contents are in the **Algarrabo duo**, which consists of Livingston (TN) (1.42) and Algarrabo (1.46); these irons plot relatively near the main group on most diagrams, but Ni and As are high, Co and Ga are low. As can be seen in Table 2 and Figures A1 and 3, concentrations of taxonomic elements, with the exception of Co, are similar in the two irons. The Ir difference is also large, a factor of 13; although Ir is of secondary value for classification, this difference is larger than could be produced by crystal segregation if D_{Ir} is around 3 to 4, as suggested in the text. The Co difference of 7% is also slightly larger than observed among MG irons having similar Au contents. Buchwald (1975) notes that the structure of Livingston (TN) implies shock and recrystallization following the initial formation of the Widmanstätten pattern, and that graphite is common. Algarrabo is paired with the new iron Ovalle; detailed structural observations are not available, but Lindner and Buchwald (1985) report that cohenite and graphite are present.

The members of the **Mundrabilla duo**, Waterville (1.63) and Mundrabilla (1.64), are FeS-rich irons, closely related to each other in structure and composition. They are within the sLL scatter field on most diagrams, but plot slightly low on the Ga-, Ge-, and W-Au diagrams. Because of these discrepancies and their very high FeS contents, we list them as ungrouped but they could also be designated anomalous members of the sLL subgroup.

The two meteorites of the **Britstown duo**, Britstown (1.93) and Elephant Moraine EET96009 (1.98) are, on most diagrams, located more or less along an extrapolation of the sLM trends to higher Au values. However, their Ga, Ge, and W values are much higher than expected from such an extrapolation. They are quite similar to each other in composition, the only moderate differences being higher contents of Ga, Ge, and W in Britstown. A striking shared characteristic is extremely high Sb contents of 2100 and 2600 ng/g. Britstown contains silicates and graphite sheaves or spherulites (Buchwald, 1975). Phases in EET96009 include silicates consisting of olivine (Fa5) and orthopy-

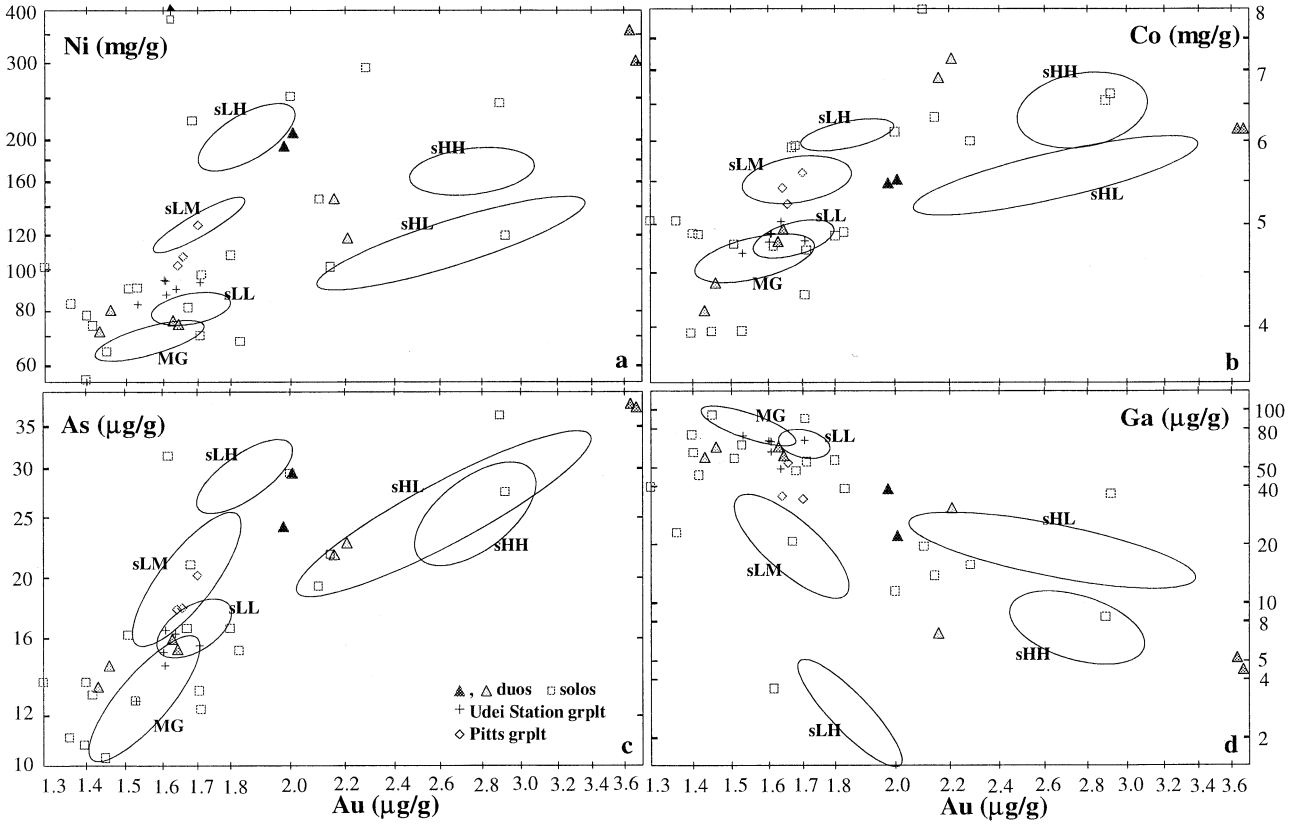

Fig. A1. Positions of the ungrouped (5 duos, 17 solos) irons are shown on the four log X–log Au plots that are most useful for classification: (a) Ni, (b) Co, (c) As, and (d) Ga. The fields of the main group and the 5 subgroups are outlined. The two low-Au grouplets are shown by small symbols.

roxene (Fs7 to 10) intergrown with sulfides and graphite (McBride et al., 2000), similar in this regard to silicate assemblages in the main group and the low-Au subgroups.

The difference in Ir is even larger (a factor of 40) between the two irons in the **NWA468 duo**, Northwest Africa NWA468 (2.21) and Grove Mountains 98003 (2.16). These two irons also differ by a factor of 4 in Ga, and the difference in Ge appears to be similar in magnitude. These differences call into question a close genetic link between the irons. The concentration of Ni is 25% lower in NWA468 than in GM98003. These irons plot close to sHH on some diagrams and close to sHL on others.

The members of the **Twin City duo** Santa Catharina (3.64) and Twin City (3.67) have very high Au contents. On several diagrams they plot near an extrapolation of the sHH or the sHL groups, but are anomalously high on the Ni, Cu, and Sb diagrams. They are compositionally very similar; they share very high Ni, Sb, and Au contents, and differ by only small degrees (10 to 30%) in Ni, Ga, Ge, and Ir. Buchwald (1975) notes that Twin City and Santa Catharina have very similar structures; both are polycrystalline ataxites in which the original taenite dimensions were 2 to 8 cm. Buchwald (1975) observed small silicates in Santa Catharina and noted that Twin City contains what appear to be silicates. He did not find carbides or graphite in either iron despite claims for graphite in the nineteenth-century literature.

A2. Seventeen Unique Meteorites

In Figs. A1 and 3 we show the positions of the 17 solo meteorites relative to the fields of the main group (MG) and the subgroups. In the following discussion we compare the compositional properties to those found in the nearest group. Low-Au meteorites are only compared to the low-Au groups, high-Au meteorites to the high-Au groups. As with the above duos, these solo irons are discussed in order of increasing Au contents.

Elephant Moraine EET84300 (1.29) has the lowest Au content. If we accept the conclusion that the (poorly determined) slopes through the subgroup fields are roughly parallel to those observed in the main group, then EET84300 could be assigned to sLM (the old IIIC); its positions on all diagrams in Figures 2 and 3 are consistent with it lying on an extrapolation of sLM to lower Au values. The reason we are not yet willing to assign EET84300 sLM is the large gap between its Au and that of the nearest "normal" member of the group, Maltahöhe, 1.60 mg/g Au (the anomalous sLM Persimmon Creek, Au = 1.53 mg/g, is slightly closer in Au). The fact that the $\Delta^{17}O$ of EET84300 is IAB-like, −0.50‰, is also in keeping with it being closely linked to the low-Au groups including sLM.

Kendall County (1.40) has by far the lowest Ni content of any meteorite in the IAB complex; its Co content is also the lowest, though only slightly lower than that in Mertzon. Both these elements plot far below the main group.

Ellicott (1.40) has the next lowest Au content. It is most closely related to the main group and the sLL subgroup, but has a high Ni content and very high Co content relative to these.

Vermillion (1.41) is a silicate-bearing iron with reduced (Fa11.5) olivine accounting for 93% of the silicates, leading to its designation as a "pyroxene pallasite" by Boesenberg et al. (2000). It plots just outside the left end of the main group on our diagrams, generally quite near Ellicott and EET84300. It is also reasonably close to an extrapolation of sLM trends to lower Au. The $\Delta^{17}O$ of the silicates is −0.76‰ (Clayton and Mayeda, 1996). Because experimental errors are relatively high for olivine-rich samples, this is within the uncertainty of the IAB range; the $\Delta^{17}O$ of Lueders is −0.68‰. Although the $\delta^{18}O$ value, 2.24‰, is ~2‰ lower than the lowest IAB values, olivine tends to have lower $\delta^{18}O$ than whole-rock chondritic silicates, thus the O-isotopic composition also appears to be consistent with Vermillion being closely related to the main group and the low-Au subgroups.

Table A1. Meteorites analyzed by INAA that we associate with the large strewn fields Campo del Cielo, Canyon Diablo, Odessa, and Toluca.

Strewn field	Compositionally similar irons received under other names
Campo del Cielo	Malequeno, Santiago del Esquero
Canyon Diablo	Albuquerque, Ashfork, Bloody Basin, Camp Verde, Cottonwood Falls, Fossil Springs, Helt Township, Houck, Las Vegas, Leverton, Mamaroneck, Moab, Pulaski County, San Luis Valley
Odessa	Honey Creek, Velarde
Toluca	California, Leeds, Masua, Moctezuma, Southern Arizona, Michigan

Yongning (1.45) is heavily weathered and, for most elements, similar to the MG in composition. The Co content is, however, 10% lower than that in main-group irons. We cannot exclude that this reflects selective weathering loss of kamacite; if so, it would require that 10 to 15% have been removed. Our small section has a high cohenite content.

Georgetown (1.51) is an unusual FeS-rich meteorite found as a number of small weathered masses in a mining region of Queensland, Australia. On most diagrams it plots near an extrapolation of sLM to lower Au contents. Its Co is much lower than the trend and its W and Ga are somewhat above such a trend, and its Cu is higher, but similar to that in the anomalous sLM member Persimmon Creek.

Mertzon (1.53) has As and Ga contents similar to those in sLL but has appreciably higher Ni and much lower Co. Solid-melt partitioning results in a positive correlation between these elements, thus the observed fractionation effectively rules out a close relationship to sLL.

Oktibbeha County (1.62) has the highest Ni content known in an iron meteorite; Ni is plotted as an upper limit in Figures 2 and A1a. Despite this very high Ni, the Co content is in the IAB-MG to sLL range.

Data on **Aswan** (1.67) cover the range of the three low-Au subgroups. Ni and As plot in sLL, Ga and Ge in sLM, Co in sLH. The two refractory lithophiles follow different trends; although Ir is relatively low, W plots above all the subgroups.

Wu-Chu-Mu-Chin (1.68) has high, sLH-like Ni and Co contents, but plots in the sLL field on Ga- and As-Au diagrams, and is thus not closely related to any group.

The **Cookeville** (1.71) data plot nearest to the MG, but Co is very low, Ni and As are low, and Ga, Ge, and W contents are higher than MG values.

The **Burkhala** (1.71) data also plot nearest the main group but Ni, Ge, and W are high, Ga is low, and As very low.

Mesa Verde Park (1.80) has a metallurgical structure closely related to the metal of Four Corners (Buchwald, 1975), which we assign to the Udei Station (US) grouplet. However, Four Corners has a high content of coarse and fine silicates (e.g., Figs. 769, 770 of Buchwald, 1975) whereas no silicates have been recognized in the structure of Mesa Verde Park (Buchwald Fig. 1146). Four Corners is the most Au-rich member of the Udei-Station grouplet, but the Mesa Verde Park value (1.64 μg/g) is still 10% higher. The Udei-Station grouplet does not produce well-defined trends on most diagrams. With this caveat in mind, the positions of Mesa Verde Park in the eight diagrams in Figs. 2 and 3 are not inconsistent with a rough extrapolation of the Udei-Station grouplet trends to higher Au contents. Nonetheless, because of the difference in silicate contents and the compositional gap, we think it best to treat Mesa Verde Park as a separate meteorite.

On most of the diagrams in Figs. and 3 **San Cristobal** (2.00) plots close to an extrapolation of the sLH trends to slightly higher Au contents. However, its Ge content is high by a factor of 10 and its Ga by a factor of 5.

Most elemental concentrations in **Ventura** (2.15) are similar to those in sHL, but the Co content is 15% higher than the sHL trend and W is 2× higher.

Samples of **Lime Creek** (2.28) are weathered and the INAA data are old and incomplete. Nonetheless these and our published RNAA data confirm that the Ni is much higher than sHH and sHL, and that the Ga and Ge values are >2× higher than the anticipated values based on extrapolations of sLH and sLM trends to the reported Au value.

Concentrations of two elements (As, Cu) in **Quesa** (2.92) are roughly similar to those in sHH and sHL; Ni is similar to sHH and Co similar to sHL. However, Ga, Ge, and W are 2× above the trends of both these groups.

A3. Origin of the Ungrouped Irons

It does not seem worthwhile in this paper to speculate on the origin of individual ungrouped irons. We suggest that most of them formed in the same fashion described above for the main group: impact-induced melting followed by minor amounts of solid-melt segregation. Because the nature of the fractionation trends cannot be determined on the basis of the positions of one or two related irons, it is not possible to confirm that the patterns are parallel to those in the main group. In many cases careful petrographic studies will reveal more information. An example is the Rubin and Wasson (2002) study of NWA468, in which they report evidence indicating that this object, which is closely related to the lodranites, formed by the impact alteration of chondritic matter.

APPENDIX B. PAIRING OF IAB IRONS

We have eliminated paired irons from Table 2. For example, we (Wasson and Ouyang, 1990) have analyzed many meteorites originally believed to be independent but that are now attributed to Canyon Diablo. Several meteorites have also been assigned to Toluca, Odessa, and Campo del Cielo. These are listed in Table A1.

There are two anomalous IAB members from eastern Europe and Russia that are remarkably similar in composition to Morasko, suggesting that they are paired with this crater-producing iron. However, the discovery description of Seeläsgen (found 94 km away) seems quite credible and Burgavli was found 5900 km away in Siberia; thus, despite sharing unusual compositions, we feel they must be treated as independent falls. More investigations are warranted, including the possibility that mislabeling in museums has occurred.

Another interesting case is Ballinger. The data listed in Table 2 were obtained on a small specimen in the UCLA collection. Another specimen from the American Museum of Natural History (AMNH) has a different composition, including 70 mg/g Ni, 85 mg/g Ga, 2.2 mg/g Ir, and 1.55 mg/g Au. D. Blakeslee (personal communication, 2001) points out that there are historical records that indicate that Wichita County was moved to its last outdoor resting site (a Native American shrine) from a location near Ballinger. Most of our data on the AMNH Ballinger are consistent with it belonging to the same fall as Wichita County, but Ir is appreciably lower (1.9 μg/g) in the latter. Our data on AMNH Ballinger are also not inconsistent with it being a stray from the Canyon Diablo strewn field.

Our data show that two Elephant Moraine irons EET87506 and EET96006 are clearly paired. Based on discovery location and metallographic examination, the Antarctic meteorite curators had already paired EET87506 with EET807504 and EET87505. A few years ago we received from C. Canut de Bon a specimen of a "new" Chilean iron called Ovalle from the Concepcion Museum. Our data show it to be identical to the Algarrabo iron meteorite.

It appears that the tiny iron previously called Thompson Brook is a piece of Mundrabilla. Thompson Brook is unresolvable from Mundrabilla in terms of our siderophile data. A. Bevan (personal communication, 2000) notes that Thompson Brook is undocumented with regard to discovery location and that its structure is consistent with it being a piece of the Mundrabilla shower.

APPENDIX C. REPLICATE ANALYSES, UNPUBLISHED OR REVISED AFTER 1986

We list in Table A2 all analyses completed between the end of 1985 and July 2001. Starting in 1986 we began using uniformly thick samples which reduced errors resulting from the self-absorption of low-energy gamma rays. We also added a fourth count that led to better precision for radionuclides with half-lives ≥1 d.

Table A2. List of 280 replicate neutron-activation analyses carried out at UCLA between Jan. 1986 and July 2001.

Meteorite	Date	Cr (μg/g)	Co (mg/g)	Ni (mg/g)	Cu (μg/g)	Ga (μg/g)	Ge (μg/g)	As (μg/g)	Sb (ng/g)	W (μg/g)	Re (ng/g)	Ir (μg/g)	Pt (μg/g)	Au (μg/g)
Alexander County	8906	30	4.56	63.3	139	94.8	461	10.5	246	1.63	297	3.65	10.0	1.440
Alexander County	8905	28	4.55	66.0	145	106	574	11.8	274	1.83	365	3.81	12.0	1.439
Algarrabo	8908	22	4.39	83.1	258	65.0	316	14.9	364	1.26	978	10.2	8.1	1.468
Algarrabo	9001	31	4.43	81.6	296	66.3	317	14.7	356	1.09	812	10.0	8.7	1.470
Algarrabo (Ovalle)	9912	32	4.42	80.4	289	65.0	294	14.2	314	0.95	942	9.82	8.9	1.458
Algarrabo (Ovalle)	9912	39	4.40	79.4	285	63.7	277	14.1	272	0.93	969	9.84	8.0	1.449
Allan Hills ALHA76002	8607	34	4.41	66.4	155	85.5	358	10.6	296	1.28	252	2.58		1.490
Allan Hills ALHA76002	8605	27	4.66	66.4	149	92.5	—	11.9	242	1.43	266	2.78		1.440
Allan Hills ALHA77283	8910	18	4.94	73.0	145	82.8	297	15.9	307	1.19	221	2.29	6.7	1.732
Allan Hills ALHA77283	9001	23	4.86	70.7	144	78.6	332	14.3	279	0.91	192	2.15	17.2	1.670
Annaheim	8601	20	4.74	79.5	527	81.4	—	13.9	502	1.74	399	3.40	—	1.520
Annaheim	8602	30	4.70	76.4	480	79.1	—	13.1	363	1.00	358	3.54	—	1.556
Anoka	8610	18	5.60	119.5	181	17.6	<100	21.4	426	<0.08	<236	0.163	<1.6	1.565
Anoka	8611	23	5.78	117.5	205	17.4	<100	19.8	535	0.11	38	0.166	<1.2	1.573
Anoka	9707	21	5.42	116.9	205	19.2	<100	23.0	471	0.11	24	0.187	1.2	1.701
Aswan	9309	15	5.91	81.0	117	21.3	<100	16.9	—	1.57	<46	0.243	13.7	1.631
Aswan	9312	21	5.94	82.9	126	21.0	<100	16.4	—	1.75	<57	0.255	10.6	1.709
Bahjoi	9005	21	4.83	77.0	158	65.4	277	16.8	422	0.95	254	2.49	5.1	1.759
Bahjoi	9312	21	4.83	80.4	134	79.6	230	17.4	660	0.97	330	2.59	6.1	1.749
Balfour Downs	8606	24	4.93	83.1	158	62.3	204	17.0	421	0.88	244	2.24	6.4	1.710
Balfour Downs	8607	21	4.81	84.4	164	57.6	183	16.2	384	1.65	239	2.09	4.7	1.680
Ballinger (AMNH)	8611	9	4.60	58.3	122	82.4	416	13.6	367	1.08	227	2.23	7.0	1.509
Ballinger (AMNH)	8612	17	4.55	66.8	141	83.1	317	13.4	283	0.96	213	2.16	7.4	1.592
Ballinger (UCLA)	8605	27	4.60	65.9	147	88.3	299	11.8	367	1.24	291	3.18	4.9	1.470
Ballinger (UCLA)	8606	26	4.62	69.8	149	87.3	416	12.3	305	1.25	348	3.21	7.9	1.510
Bischtübe	8601	23	5.05	69.2	139	68.4	—	17.6	333	0.79	211	2.35		1.620
Bischtübe	8604	22	5.06	69.6	132	66.5	212	16.8	363	0.69	238	2.40		1.740
Bischtübe	8610	25	4.83	76.7	138	68.1	199	16.5	370	0.63	182	2.22	5.7	1.694
Bitburg	8606	110	7.77	181	546	30.1	199	35.3	1200	<0.15	<100	1.24	4.7	3.25
Black Mountain	8604	27	4.74	58.9	121	96.4	483	12.1	302	1.42	344	2.87		1.530
Black Mountain	8606	19	4.58	64.8	135	95.4	472	11.9	240	1.44	332	2.96	9.2	1.500
Bocaiuva	0107	176	4.12	86.5	260	18.2	<100	9.8	898	1.12	416	3.53	6.3	0.840
Bogou	8603	24	4.67	74.7	164	81.6	292	14.3	320	1.15	210	1.73	3.7	1.650
Bogou	8607	23	4.66	71.8	162	77.4	279	14.1	288	1.03	184	1.71	5.9	1.640
Bohumilitz	8601	24	4.81	71.1	137	81.2	—	15.7	345	0.94	210	2.04		1.500
Bohumilitz	8603	18	4.71	72.6	131	74.9	305	15.0	370	0.82	230	2.03		1.690
Bolivia	8605	<20	4.76	68.4	162	98.8	438	11.0	284	1.26	221	2.09	7.4	1.510
Bolivia	9005	21	4.48	67.2	159	99.5	456	12.2	278	1.47	246	2.04	8.8	1.432
Burkhala	9004	48	4.68	100.8	486	57.6	441	12.4	632	1.73	753	7.82	11.3	1.930
Burkhala	9005	81	4.77	93.6	435	50.3	434	12.2	677	1.47	765	8.24	13.5	1.602
Caddo County	8809	29	4.79	95.8	350	66.7	253	13.1	340	0.88	237	2.48	4.2	1.608
Caddo County	9005	343	5.11	91.0	357	71.7	<400	17.3	511	1.40	388	2.62	10.9	1.605
Campo d. Ci (Malequeno)	9604	50	4.54	67.1	174	107	<200	13.3	450	1.49	500	3.64	9.1	1.527
Campo d. Ci (Malequeno)	9605	41	4.66	65.3	149	93.1	406	11.7	280	1.13	250	3.51	7.5	1.537
Campo d. Ci (Sant.d.Estero)	9810	11	4.68	65.6	142	94.8	400	12.3	237	1.42	419	3.88	7.7	1.494
Campo d.C (El Taco)	8612	47	4.47	69.0	132	89.7	377	10.8	272	1.24	315	3.23	6.7	1.402
Campo d.Ci (Sant.d.Estero)	9903	44	4.53	67.4	133	91.2	316	11.1	212	1.32	363	3.77	8.0	1.476
Campo del Cielo	8604	31	4.52	69.4	138	93.9	382	11.3	288	1.32	291	3.22	6.7	1.460
Canyon Di (Albuquerque)	9412	24	4.86	74.4	149	80.3	319	12.9	283	0.95	157	2.24	5.9	1.62
Canyon Di (Mamaroneck)	8705	33	4.48	67.9	173	80.5	361	12.1	407	1.36	264	2.53	6.6	1.479
Canyon Di (Mamaroneck)	8910	20	4.80	68.2	148	86.5	329	14.7	436	0.95	252	2.51	5.9	1.608
Canyon Di (San Luis Valley)	9906	31	4.70	67.2	138	81.9	347	13.0	263	1.03	250	2.46	5.9	1.486
Canyon Di (San Luis Valley)	9908	38	4.59	69.6	149	81.7	283	13.0	238	0.97	237	2.44	6.4	1.520
Canyon Di Pulaski County	8910	28	4.34	67.6	159	78.5	325	12.2	254	1.20	208	2.11	6.2	1.492
Canyon Di Pulaski County	9001	22	4.93	70.5	167	86.2	368	12.7	297	0.86	216	2.26	6.9	1.639
Carlton	8607	18	5.60	132.0	248	11.7	<100	23.3	512	<0.10	<10	0.080		1.700
Casey County	8604	22	4.85	75.5	160	82.7	312	14.0	400	1.17	152	1.42		1.630
Chuckwalla	9307	26	4.63	67.9	161	104	284	22.1	470	1.65	180	2.91	9.3	1.591
Chuckwalla	9312	26	4.68	61.8	144	95.3	492	11.0		1.47	294	2.62	7.4	1.397
Chuckwalla	9412	31	4.51	66.0	156	100.6	480	11.8	133	1.57	256	2.62	9.0	1.441
Colfax	8601	20	5.22	108.0	352	55.5	—	18.1	563	0.55	149	1.77		1.650
Colfax	8602	20	5.22	104.0	315	53.7	—	17.7	513	0.43	123	1.72		1.660
Comanche (iron)	8610	22	5.31	88.5	178	81.2	266	18.5	388	0.91	232,860		6.5	1.698
Comanche (iron)	8611	18	4.99	86.8	199	79.8	319	17.5	471	0.95	219	2.950	6.3	1.883
Cookeville	8601	29	4.35	69.1	147	84.5	—	12.6	292	1.07	275	2.38		1.620

(continued)

Table A2. (Continued)

Meteorite	Date	Cr (μg/g)	Co (mg/g)	Ni (mg/g)	Cu (μg/g)	Ga (μg/g)	Ge (μg/g)	As (μg/g)	Sb (ng/g)	W (μg/g)	Re (ng/g)	Ir (μg/g)	Pt (μg/g)	Au (μg/g)
Cookeville	8603	24	4.30	65.8	149	88.9	423	14.0	290	1.16	260	2.46		1.810
Cookeville	8612	33	4.21	76.1	167	91.9	386	13.1	278	1.30	216	2.54	8.9	1.699
Coolac	8604	35	4.57	70.6	158	92.5	379	11.1	246	1.45	347	2.86		1.470
Coolac	8605	36	4.45	69.1	163	94.5	451	11.0	306	1.38	251	2.82	8.1	1.500
Copiapo	8602	97	4.72	73.8	167	71.4	—	14.3	270	0.98	284	3.02		1.661
Dayton	9511	12	5.83	175	445	5.00	<100	26.0	597	0.24	<55	0.027	1.4	1.741
Dayton	9601	13	6.01	168	424	4.48	<190	24.4	770	<0.16	<86	0.028	<3.2	1.730
Deelfontein	8603	25	3.85	71.7	176	89.9	320	15.1	390	5.67	250	1.62	3.8	1.680
Deelfontein	8607	37	4.82	65.3	146	70.2	276	11.0	187	1.95	154	1.44	4.9	1.450
Deelfontein	8611	19	5.19	78.3	173	99.2	435	17.6	459	1.45	135	1.74	5.2	1.780
Dongling	8605	17	4.87	71.3	160	86.4	239	13.5	303	0.92	143	1.79	4.0	1.510
Duel Hill (1873)	8610	13	4.75	66.1	247	102.5	431	12.1	285	1.47	388	4.23	10.1	1.455
Duel Hill (1873)	9306	20	4.63	68.4	150	99.5	500	12.1	299	1.76	307	4.35	7.3	1.434
Duel Hill (1873)	9312	28	4.56	66.9	175	99.2	457	11.7		1.47	430	4.23	9.1	1.428
Dungannon	8612	27	4.85	71	110	73.1	275	12.3	374	0.96	199	2.61	5.6	1.427
Dungannon	8607	25	4.54	65.2	137	85.6	320	12.6	270	1.09	227	2.52	4.6	1.540
Elephant Mor EET83333	8608	39	4.88	78.7	255	70.9	281	14.7	406	0.81	239	2.88	8.8	1.723
Elephant Mor EET83333	8610	9	4.78	81.9	202	76.8	266	16.6	443	0.79	276	2.84	6.2	1.742
Elephant Mor EET84300	8608	130	5.00	103.0	185	39.0	104	13.3	320	0.34	155	1.70	3.1	1.241
Elephant Mor EET84300	8610	29	5.07	99.1	205	40.9	<100	13.9	412	0.30	171	1.96	<3.2	1.330
Elephant Mor EET87506	8908	35	5.35	208.2	939	22.6	119	29.1	2754	0.36	267	3.06	5.9	1.949
Elephant Mor EET87506	9001	56	5.23	209.0	1190	23.1	145	29.4	2770	0.42	241	2.95	10.1	1.964
Elephant Mor EET96009	0008	13	5.60	209.6	1029	22	<150	29.1	2680	0.38	297	3.12	5.1	1.980
Elephant Mor EET96009	0009	50	5.43	206.2	1118	22.6	116	29.9	2576	0.26	293	3.12	5.7	2.033
Ellicott	8601	18	5.02	75.4	175	61.5	—	14.1	135	1.41	328	3.45		1.430
Ellicott	8602	18	4.80		175	61.5	—	13.1	242	1.59	291	3.47		1.380
Faifield, OH	8804	20	4.59	69.0	150	79.0	337	12.9	295	1.02	181	1.80	6.1	1.568
Fairfield, OH	8806	18	4.81	65.4	137	82.4	366	13.3	235	1.04	140	1.77	5.5	1.506
Föllinge	8611	11	5.95	173.4	374	3.86	<100	26.0	952	<0.08	<27	0.108	<1.1	1.720
Föllinge	8612	13	5.96	179.1	368	3.90	<100	26.7	724	<0.06	<21	0.104		1.680
Four Corners	8612	49	5.05	88.5	262	47.7	188	15.6	550	0.57	205	2.46	5.5	1.647
Four Corners	8705	10	5.01	96.4	257	51.7	146	16.9	450	0.65	258	2.39	5.2	1.625
Freda	8709	11	6.30	232.6	662	2.18	<100	29.8	1313	<.094	<81	0.019	<2.3	1.900
Freda	8801	10	6.19	237.9	679	2.08	<100	30.3	1090	<.08	<30	0.012	<1.8	1.890
Gahanna	9412	22	4.75	67.9	165	85.3	333	13.7	262	0.94	154	1.82	7.5	1.591
Gahanna	9503	13	4.57	70.7	182	85.5	—	12.5	430	0.98	287	1.91	4.5	1.603
Garden Head	0101	7	6.01	168.4	394	10.3	<100	22.1	248	0.13	<30	0.135	1.8	2.34
Gay Gulch	0101	9	6.74	144.5	261	6.16	<125	25.4	338	0.51	<50	0.100	3.5	2.47
Georgetown	9306	2790	5.12	90.1	347	58.3	251	18.4	370	0.72	<45	0.251	3.6	1.518
Georgetown	9307	4340	4.61	75.8	573	45.6	—	14.2		0.72	<51	0.210	2.9	1.322
Georgetown	0105	1611	4.64	97.7	262	59.0	208	16.0	473	0.50	12	0.240	2.6	1.571
Gladstone (iron)	8602	18	4.80	64.0	149	90.8	—	11.2	306	1.55	318	3.06		1.480
Goose Lake	8906	36	4.89	85.5	180	68.4	263	16.3	414	0.88	211	2.14	5.9	1.660
Goose Lake	8908	26	4.81	85.5	160	70.9	285	16.3	395	1.79	210	2.15	5.7	1.638
Goose Lake	8910	30	4.88	78.4	167	68.8	251	16.6	365	0.91	214	2.17	6.2	1.611
Grosvenor Mtn GRO95511	9903	22	4.85	82.0	198	71.9	255	16.1	373	0.88	186	2.00	5.5	1.722
Grosvenor Mtn GRO95511	9904	16	4.88	81.5	195	73.6	242	16.5	323	0.84	186	1.97	7.0	1.667
Grove Mountains 98003	0002	13	6.94	144.8	375	6.75	<100	21.8	408	0.62	<40	0.070	5.8	2.11
Grove Mountains 98003	0004	11	6.84	147.8	366	7.16	<100	21.8	400	0.58	<66	0.065	5.9	2.21
Guangxi Coal Mine	9808	24	4.63	69.1	158	85.3	410	13.4	332	0.98	210	1.86	6.0	1.558
Guangxi Coal Mine	9903	25	4.59	72.2	173	83.9	356	13.6	371	1.06	165	1.83	4.6	1.605
Gun Creek	9905	12	5.07	82.1	108	22.2	<100	10.8	<200	0.27	<31	0.061	3.3	1.302
Harlowtown	8610	21	4.87	86.8	294	61.1	180	17.0	353	0.63	260	2.73	6.7	1.599
Hassi-Jekna	8611	17	5.69	103.9	180	23.2	<100	27.2	436	0.20	<32	0.212	1.6	2.30
Hassi-Jekna	8612	18	5.37	112.7	174	21.9	<100	25.9	265	0.22	<19	0.263	1.4	2.50
Idaho	8603	24	4.66	72.7	149	84.5	312	13.5	333	1.08	233	2.62	3.7	1.550
Idaho	8604	23	4.65	72.6	156	82.0	265	12.9	274	1.03	258	2.50	9.5	1.533
Idaho	8806	24	4.68	72.8	156	86.0	353	13.2	259	1.06	264	2.51	5.6	1.546
Itapuranga	8610	28	4.68	63.7	120	94.0	508	11.5	289	1.27	220	2.54	9.7	1.480
Jaralito	8604	33	4.34	70.3	150	85.8	329	10.4	280	1.26	152	1.47		1.500
Jenkins	8603	18	4.64	68.4	150	87.1	410	12.6	370	1.02	270	2.12		1.570
Jenkins	8604	31	4.59	74.0	158	90.0	342	13.1	319	1.26	255	2.23		1.640
Jenny's Creek	8608	22	4.65	72.1	—	—	—	—	309	—	—	2.56	8.4	1.728
Jenny's Creek	8611	24	4.74	67.6	149	85.2	304	14.1	392	1.01	240	2.36	5.8	1.534
Jenny's Creek	8704	19	4.71	65.6	133	76.8	310	13.1	363	1.26	303	2.40	5.7	1.540

(continued)

Table A2. (Continued)

Meteorite	Date	Cr (μg/g)	Co (mg/g)	Ni (mg/g)	Cu (μg/g)	Ga (μg/g)	Ge (μg/g)	As (μg/g)	Sb (ng/g)	W (μg/g)	Re (ng/g)	Ir (μg/g)	Pt (μg/g)	Au (μg/g)
Kaalijarv	9412	28	4.81	75.3	165	82.1	311	17.0	455	1.00	226	3.07	8.0	1.712
Kaalijarv	9503	17	4.70	75.5	153	78.2	—	18.0	690	0.87	266	3.00	<3.6	1.641
Karee Kloof	8608	45	4.76	84.8	228	81.7	341	14.7	440	1.18	102	1.34	9.0	1.539
Karee Kloof	8607	36	4.64	81.8	227	75.8	274	14.0	480	1.31	92	1.26	6.5	1.580
Kendall County	8611	189	3.94	57.6	454	76.6	360	10.5	721	0.93	243	2.18	9.3	1.372
La Serena	9003	18	4.75	77.0	199	70.6	190	16.1	380	0.66	80	0.549	3.2	1.690
La Serena	9004	15	4.77	75.3	162	70.4	246	15.6	362	0.66	<48	0.547	3.4	1.640
Lamesa	8607	14	5.59	134.0	316	12.9	<100	24.9	588	<0.04	≯30	0.048	<0.6	1.690
Landes	8604	433	4.44	66.4	635	89.2	487	10.6	238	1.39	293	4.24		1.450
Landes	8801	473	4.51	64.7	319	82.6	485	9.18	274	1.35	416	4.23	12.5	1.392
Lewis Cliff LEW 86540	8908	12	5.93	187.1	459	4.31	<100	29.6	37	<0.08	<30	0.044	<1.3	1.806
Lewis Cliff LEW 86540	9001	12	6.05	178.7	498	4.29	<100	27.9	730	<0.06	<21	0.043	2.0	1.820
Linville	0105	11	6.16	156.6	276	8.30	<100	31.5	336	0.11	<37	0.018	1.6	3.06
Linwood	8602	14	4.47	69.0	137	88.5	—	11.8	271	1.16	288	2.88		1.484
Livingston TN	8804	31	4.12	73.5	297	60.5	288	13.4	239	0.82	90	0.812	4.2	1.431
Livingston TN	8806	34	4.14	76.7	296	64.7	258	13.4	548	0.84	78	0.783	5.2	1.391
Lueders	9412	429	4.75	70.4	304	80.8	464	12.1	308	1.28	273	3.91	6.5	1.519
Lueders	9503	333	4.55	70.7	405	79.5	372	12.2	380	1.18	300	3.87	6.6	1.494
Magnesia	8602	22	5.35	108.0	256	14.3	<100	24.0	224	0.22	<48	0.140		2.71
Magura	8602	32	4.57	64.3	138	98.3	—	10.5	172	1.66	347	3.71		1.445
Maltahöhe	9103	14	5.35	101.9	172	25.3	<100	19.1	482	0.16	<50	0.180	1.2	1.623
Maltahöhe	9204	15	5.17	125.3	154	22.7	<100	19.3		0.23	34	0.161	2.5	1.321
Mayerthorpe	8603	21	4.76	69.4	139	80.5	261	15.5	320	1.62	240	2.15	3.1	1.620
Mayerthorpe	8604	27	4.74	72.3	138	77.3	332	14.7	305	0.94	229	2.22		1.660
Mazapil	8605	<25	4.96	87.8	222	57.0	228	17.0	408	0.77	389	5.49		1.700
Mazapil	0101	17	4.90	89.2	192	57.5	325	17.6	354	0.64	395	5.69	10.1	1.689
Mertzon	8602	70	4.19	94.0	668	65.4	—	12.5	560	0.90	180	2.30		1.540
Mesa Verde Park	8612	22	4.73	126.0	349	54.0	125	16.5	502	0.58	226	2.11	4.3	1.993
Mesa Verde Park	8705	13	5.02	105.6	300	58.5	184	16.7	436	0.50	293	2.21	5.4	1.703
Misteca	8612	91	5.51	83.7	172	68.2	256	18.1	440	0.80	305	3.16	7.1	1.872
Misteca	8608	27	5.62	88.2	166	70.7	352	19.3	522	0.70	279	2.77	8.0	2.07
Misteca	8607	20	4.99	80.3	166	66.0	225	17.4	549	0.73	205	2.05		2.46
Misteca	8608	22	5.74	90.8	172	73.6	378	21.0	557	0.73	313	2.75		2.13
Misteca	8612	93	5.58	82.3	167	66.6	260	18.3	433	0.78	318	3.18	7.1	1.870
Morrill	8608	14	4.80	84.5	299	67.0	291	16.1	435	0.93	198	2.05	7.9	1.640
Morrill	8607	18	4.78	79.5	254	61.6	260	15.1	419	0.91	188	1.85	6.5	1.640
Mount Ayliff	9312	23	4.92	69.2	125	80.1	308	15.5		0.79	280	2.26	5.4	1.632
Mount Ayliff	9412	28	4.83	69.4	142	85.9	355	15.9	287	0.92	228	2.21	8.4	1.633
Mount Howe HOW88403	9008	###	4.31	88.1	389	22.4	<100	11.9		0.93	560	4.67	8.8	1.234
Mount Howe HOW88403	9103	598	4.36	84.1	374	21.7	<100	11.9	248	0.99	529	4.72	7.1	1.265
Mundrabilla	8601	124	4.97	78.1	116	60.6	—	16.7	421	0.53	115	0.910		1.610
Mungindi	8704	15	5.51	121	253	18.2	<33	22.5	466	<0.07	76	0.590	<1.0	1.720
Mungindi	8709	14	5.48	120	243	18.7	<50	22.2	496	<0.07	<410	0.575	1.5	1.610
Nagy-Vazsony	8906	21	4.94	80.4	189	72.5	263	18.2	422	0.88	282	2.25	5.9	1.730
Nagy-Vazsony	8910	15	5.05	82.5	188	75.3	284	18.2	419	0.75	271	2.79	6.3	1.841
Nantan	8605	20	4.69	70.2	149	83.1	321	13.0	319	1.00	158	1.75	6.3	1.490
Neptune Mountains	8601	24	4.75	70.1	149	77.0	—	14.1	290	0.90	162	2.21		1.590
Neptune Mountains	8603	22	4.70	74.0	148	79.4	254	14.7	340	0.92	240	2.18	3.6	1.660
New Leipzig	8602	25	4.64	65.5	150	93.6	—	11.3	202	1.44	280	2.97		1.422
Niagara	8902	11	5.34	77.5	164	72.7	244	17.5	377	0.78	293	2.94	5.4	1.781
Niagara	8906	17	4.85	80.2	180	71.9	291	16.5	378	0.82	245	2.50	6.1	1.745
North West Africa NWA176	0011	523	4.14	86.6	318	17.7	137	9.12	133	1.02	359	3.56	7.8	0.853
North West Africa NWA176	0101	337	4.14	85.4	281	19.7	439	9.72	66	1.29	351	3.67	9.2	0.870
North West Africa NWA468	0004	###	7.22	119.2	282	31.3	124	22.9	421	0.62	292	2.80	4	2.25
North West Africa NWA468	0006	45	7.16	117.8	243	30.6	109	22.7	441	0.67	270	2.70	3.9	2.17
Ocotillo	9008	19	4.69	70.1	112	74.1	300	13.9	332	0.84	302	2.60	4.9	1.650
Ocotillo	9103	26	4.60	71.6	120	70.4	276	13.5	326	0.78	213	2.61	6.0	1.679
Ogallala	9312	29	4.76	80.8	155	68.1	309	15.7	373	1.02	310	2.42	6.6	1.629
Ogallala	9412	31	4.92	78.3	142	69.4	292	16.1	308	1.12	212	2.43	4.8	1.643
Oscuro Mountains	8606	25	4.36	70.3	157	76.6	317	11.8	265	1.24	268	2.95	5.4	1.500
Osseo	8606	23	4.61	67.1	161	92.4	463	11.1	287	1.62	610	6.04		1.560
Ozren	9312	27	4.80	69.3	134	79.6	331	14.2		1.10	194	2.61	4.0	1.569
Ozren	9412	35	4.69	72.4	144	77.4	368	13.9	230	0.94	200	2.58	5.6	1.602
Pan de Azucar	8603	24	4.70	67.7	166	80.6	332	12.1	310	1.11	290	2.75	3.6	1.500
Pan de Azucar	8606	32	4.70	71.9	176	87.6	386	12.5	294	1.17	318	2.91		1.560

(continued)

Table A2. (Continued)

Meteorite	Date	Cr (μg/g)	Co (mg/g)	Ni (mg/g)	Cu (μg/g)	Ga (μg/g)	Ge (μg/g)	As (μg/g)	Sb (ng/g)	W (μg/g)	Re (ng/g)	Ir (μg/g)	Pt (μg/g)	Au (μg/g)
Pecora Escarp PCA91003	9306	32	4.61	67.9	134	78.6	313	12.8	240	1.09	335	3.63	5.8	1.408
Pecora Escarp PCA91003	9307	25	4.63	73.6	162	86.5	—	13.1	610	1.13	210	3.59	5.9	1.599
Pine River	8607	8	4.49	90.5	153	53.1	177	12.1	380	0.66	242	3.01	5.0	1.360
Pine River	8610	8	4.86	80.3	211	75.3	205	16.0	315	0.68	285	3.04	5.3	1.637
Pine River	8704	14	4.84	84.3	227	69.8	254	15.4	413	0.70	310	3.06	4.6	1.620
Pitts	8607	14	5.98	122	394	34.7	102	19.8	926	0.39	132	1.17	3.1	1.780
Pitts	8610	14	5.47	131.3	383	35.8	64	20.6	896	0.30	83	1.27	<1.9	1.660
Pittsburg	8608	20	4.62	73.0	145	92.1	374	14.6	322	1.13	269	2.12	7.5	1.640
Pittsburg	8610	12	4.73	63.5	120	92.4	379	14.6	260	1.03	200	2.13	5.4	1.621
Pooposo	8607	44	4.64	68.1	188	78.9	309	11.7	324	1.06	235	2.68		1.510
Purgatory Peak A77006	8709	13	4.68	74.3	154	79.2	293	14.4	402	0.92	204	2.32	5.5	1.618
Purgatory Peak A77006	8910	23	4.71	70.0	153	77.0	272	14.7	287	0.93	223	2.26	5.4	1.507
Quesa	0105	17	6.90	124.4	164	38.2	<100	31.0	117	0.53	<35	0.087	<1.5	3.03
Redfields	8804	55	4.87	68.4	97	38	<100	15.5	108	0.54	89	1.016	3.1	1.839
Redfields	8806	54	4.93	69.4	98	40.3	107	15.5	108	0.57	125	0.955	2.6	1.841
Redfields	8809	57	4.95	66.7	92	38.9	100	14.8	151	0.49	101	0.932	<1.9	1.809
Rifle	8603	29	4.69	69.6	137	78.5	308	14.6	310	0.81	230	1.940	3.3	1.640
Rifle	8902	22	4.73	69.1	128	73.5	288	14.2	342	0.85	204	1.936	5.8	1.566
Rifle	8904	25	4.68	71.2	136	77.1	276	14.5	319	0.85	223	1.959	5.5	1.586
Rosario	8602	24	4.66	68.1	149	87.3	—	11.8	237	1.09	196	1.88		1.554
San Cristobal	8704	17	6.22	249	934	11.1	<100	28.9	2168	<0.09	<33	0.324	<2.9	2.050
San Cristobal	9412	16	6.02	255.2	953	11.5	<120	30.0	2141	0.18	<43	0.334	2.3	1.947
Santa Catharina	8601	10	6.14	375.0	1398	5.01	<100	38.2	2670	0.28	<132	0.030		3.65
Sardis	8601	19	4.66	64.4	136	96.2	—	12.0	251	1.29	250	2.02		1.480
Sardis	8603	17	4.56	70.1	140	100	472	12.2	300	1.31	280	2.00	5.7	1.560
Sarepta	8602	12	4.68	65.8	147	99.8	—	11.6	387	1.36	415	4.36		1.461
Seligman	8611	35	4.50	67.5	159	90.4	457	11.8	332	1.26	294	3.27	7.2	1.442
Seymour	8602	33	4.64	68.1	160	87.1	—	12.8	204	1.01	202	1.73		1.580
Shrewsbury	8601	20	4.94	84.8	218	61.9	—	17.2	431	0.59	251	2.81		1.720
Shrewsbury	8603	13	4.88	86.8	215	64.0	160	17.3	430	0.62	270	2.74	3.2	1.780
Silver Crown	8603	26	4.61	69.7	143	83.4	320	12.6	300	1.02	300	2.76		1.630
Silver Crown	8604	31	4.61	75.4	142	84.8	288	12.9	323	1.00	281	2.85		1.690
Smithville	8612	21	4.60	70.5	156	87.5	329	13.3	361	0.86	215	1.91	5.7	1.570
Soledade	8610	20	4.70	64.8	130	96.2	390	11.2	290	1.35	378	3.91	8.3	1.470
Soledade	8611	22	4.43	70.8	164	101	450	11.0	351	1.50	407	3.88	11.0	1.460
Soroti	8809	18	6.48	133.6	331	12.9	<100	23.9	578	<0.16	<24	0.006	<0.9	1.566
Surprise Springs	9312	39	4.75	81.3	191	65.4	221	14.3	400	0.72	240	2.36	4.6	1.686
Surprise Springs	9412	34	4.94	77.6	195	71.2	325	17.6	385	0.84	244	2.37	4.6	1.621
Tazewell	8612	13	5.91	170.1	367	4.70	<100	26.4	730	<0.04	<14	0.094	<2.7	1.680
Thiel Mountains TIL91725	9306	232	4.63	84.3	170	75.4	243	13.2	502	1.04	283	3.68	7.5	1.515
Thiel Mountains TIL91725	9307	185	4.76	76.5	178	71.8	—	12.2	480	1.00	210	3.65	4.8	1.542
Thompson Brook	8704	18	5.03	76.5	136	59.7	184	17.0	435	0.62	109	1.04	4.3	1.660
Toluca Nueva	8804	64	4.89	79.9	223	55.5	201	15.7	305	0.66	188	1.69	4.4	1.632
Toluca Nueva	8806	37	4.77	84.4	287	60.6	218	15.3	347	0.69	166	1.57	5.2	1.726
Twin City	0101	7	5.96	306.2	1154	4.38	<100	39.1	2240	0.07	<77	0.021	2.2	3.64
Udei Station	8611	58	4.87	98.8	256	68.8	184	15.1	607	0.59	148	0.687	3.6	1.563
Uruacu	9908	29	4.65	64.7	148	91.0	345	11.8	251	1.26	322	3.36	8.7	1.472
Uruacu	9909	28	4.67	63.8	142	88.3	370	11.4	290	1.25	332	3.37	8.9	1.444
Vermillion	9511	20	4.86	76.4	121	47.9	140	13.3	<200	0.60	234	2.02	3.3	1.446
Vermillion	9503	61	4.89	73.5	123	44.4	—	12.7	<500	0.57	240	1.90	<2.0	1.383
Victoria West	8709	13	5.70	125.6	157	16.3	<100	28.9	420	0.20	<22	0.035	2.8	2.814
Waldron Ridge	9003	39	4.71	77.8	261	78.1	297	11.7	270	10.2	220	2.22	6.4	1.487
Waldron Ridge	9005	37	4.60	81.4	291	77.9	356	12.3	330	5.14	256	2.22	6.6	1.504
Waterville	8601	503	4.78	76.3	151	65.6	—	15.5	432	0.68	41	0.38	—	1.604
Waterville	0105	57	4.89	77.3	154	71.4	204	16.4	300	0.79	30	0.373	3.1	1.681
Wedderburn	0107	10	6.12	232.0	529	1.41	<100	32.7	1190	<0.09		0.058	2.4	1.997
Wolsey	9103	51	4.57	66.1	121	85.3	428	9.92	224	1.51	408	4.79	9.8	1.378
Wolsey	9104	35	4.47	66.2	153	100	489	11.0	292	1.61	546	4.93	10.7	1.536
Woodbine	8606	101	5.54	97.5	163	34.8	140	18.2	540	0.74	244	2.02	6.0	1.520
Woodbine	8607	50	5.30	92.6	171	36.0	120	17.4	505	0.47	173	1.93	4.7	1.700
Wu-Chu-Mu-Chin	9808	10	5.90	225.1	837	46.6	111	20.3	845	0.64	263	2.68	6.8	1.704
Wu-Chu-Mu-Chin	9806	20	5.97	218.3	764	49.7	245	21.7	750	0.87	260	2.59	6.3	1.658
Yenberrie	8604	23	4.64	73.8	164	84.3	324	12.7	282	1.09	370	3.49		1.550
Yenberrie	8605		4.79	67.5	153	80.8	299	12.4	451	0.97	278	3.52	5.7	1.520
Yongning	0101	43	3.74	63.3	151	89.1	821	9.66	215	2.17	426	4.24	11.2	1.425

(continued)

Table A2. (Continued)

Meteorite	Date	Cr (μg/g)	Co (mg/g)	Ni (mg/g)	Cu (μg/g)	Ga (μg/g)	Ge (μg/g)	As (μg/g)	Sb (ng/g)	W (μg/g)	Re (ng/g)	Ir (μg/g)	Pt (μg/g)	Au (μg/g)
Youndegin (IN0019)	8601	26	4.90	61.2	126	82.7	—	12.7	258	1.18	213	2.23		1.400
Youndegin (IN0019)	8605	31	4.55	73.4	169	89.8	356	13.5	297	1.13	218	2.11	5.1	1.550
Youndegin (IN1167)	8605	31	4.62	69.4	151	84.4	350	12.7	306	1.07	222	2.09	5.2	1.500
Youndegin (IN1168)	8605	21	4.83	70.8	153	89.1	391	13.8	401	0.99	211	2.17	5.9	1.680
Youndegin (WAM)	8704	29	4.66	66.9	141	81.4	324	12.2	258	1.06	244	2.08	4.7	1.490
Youndegin (WAM)	8705	23	4.62	68.8	146	83.6	390	12.5	381	1.06	188	2.27	6.4	1.565
Zaffra	8604	25	4.79	77.1	160	73.9	221	15.2	323	0.73	<33	0.06		1.670
Zagora	8801	146	4.95	98.7	199	61.4	<240	13.8	336	1.02	231	2.58	7.0	1.417
Zagora	8804	9	4.72	91.6	313	72.7	289	15.8	368	0.77	295	2.87	6.2	1.787
Zagora	0101	36	4.81	90.6	288	73.2	227	16.4	347	0.87	271	2.93	6.0	1.749
Zapaliname	0002	24	4.65	67.6	138	87.9	348	12.5	251	1.20	196	1.81	6.2	1.495
Zapaliname	0006	37	4.50	66.5	122	80.4	316	11.1	218	1.33	207	1.82	5.5	1.436
Ziz	0006	26	4.68	69.1	138	90.9	379	11.1	354	1.11	213	2.10	6.8	1.499
Ziz	0011	33	4.40	65.9	142	87.3	424	10.2	180	1.29	207	2.03	6.9	1.423